

## Anelastic convection-driven dynamo benchmarks

C.A. Jones<sup>a,\*</sup>, P. Boronski<sup>a</sup>, A.S. Brun<sup>b</sup>, G.A. Glatzmaier<sup>c</sup>, T. Gastine<sup>d</sup>, M.S. Miesch<sup>e</sup>, J. Wicht<sup>d</sup>

<sup>a</sup> Department of Applied Mathematics, University of Leeds, Leeds LS2 9JT, UK

<sup>b</sup> Laboratoire AIM Paris-Saclay, CEA/IRFU, Université Paris-Diderot CNRS/INSU, 91191 Gif-sur-Yvette, France

<sup>c</sup> Department of Earth and Planetary Sciences, University of California Santa Cruz, CA 95064, USA

<sup>d</sup> Max Planck Institute for Solar System Research, Max-Planck-Str. 2, 37191 Katlenburg-Lindau, Germany

<sup>e</sup> High Altitude Observatory, National Center for Atmospheric Research, P.O. Box 3000, Boulder, CO 80307-3000, USA

### ARTICLE INFO

#### Article history:

Received 15 May 2011

Revised 9 August 2011

Accepted 15 August 2011

Available online 25 August 2011

#### Keywords:

Magnetic fields

Jovian planets

Interiors

### ABSTRACT

Benchmark solutions for fully nonlinear anelastic compressible convection and dynamo action in a rotating spherical shell are proposed. Three benchmarks are specified. The first is a purely hydrodynamic case, which is steady in a uniformly drifting frame. The second is a self-excited saturated dynamo solution, also steady in a drifting frame. The third is again a self-excited dynamo but is unsteady in time, and it has a higher Rayleigh number than the steady dynamo benchmark. Four independent codes have been tested against these benchmarks, and very satisfactory agreement has been found. This provides an accurate reference standard against which new anelastic codes can be tested.

© 2011 Elsevier Inc. All rights reserved.

### 1. Introduction

The anelastic approximation can be usefully employed to study convection in giant planets and stars, including the Sun. In these bodies, the heat flux emerging from the interior is often carried by convection. This heat flux is usually sufficiently small that only subsonic velocities are required to transport it. However, Boussinesq models are not really adequate to describe the convection, because the density in giant planets and stars is much greater in their deep interiors than in their upper regions. Fully compressible convection models suffer from the disadvantage that they allow sound waves which have oscillation periods of typically only minutes. The turnover time of the convection, and the timescale on which magnetic field is generated by dynamo action, are much longer than this. The existence of these two very different timescales makes numerical simulation very difficult, as a vast number of timesteps is required if they have to be short enough to resolve sound waves, while the time integration has to last many turnover times. In practice, the difficulty can be even worse if dynamo action is considered, as it may be necessary to integrate for at least a substantial fraction of a magnetic diffusion time (and often several diffusion times, which may need to be turbulent eddy diffusion times in astrophysical applications) before the magnetic field reaches its fully saturated state. The anelastic approximation, which filters out sound waves and so allows a much larger

timestep, is therefore a popular choice for studies of solar and stellar convection zones and the interior dynamics of giant planets (e.g. Glatzmaier, 1984, 1985; Brun et al., 2004; Jones et al., 2009; Jones and Kuzanyan, 2009; Miesch et al., 2000; Kaspi et al., 2009).

To model the convection zones of planets and stars, a spherical shell geometry is natural, and rotation usually strongly influences the dynamics. Fully three-dimensional anelastic models are typically more expensive to run than Boussinesq models, as the variation in density often leads to smaller spatial scales requiring higher resolution. The recent development of relatively inexpensive parallel computer clusters now makes it more practical to use anelastic codes to explore the dynamics of convection zones, and this has led to the construction of a number of different anelastic codes. Verifying these codes is not a simple matter, and the main purpose of this paper is to provide researchers with some straightforward benchmark cases that have been independently checked. This work is a natural follow-up from the benchmark published for the Boussinesq dynamo problem by Christensen et al. (2001). Another aim was to compare the results of some already existing codes. The community decision to develop these benchmark tests was taken at the *Kavli Institute of Theoretical Physics* programme on 'Dynamo theory' in 2008. A dynamo benchmark that is steady in a drifting frame evolves to a state with time-independent values of the kinetic and magnetic energy, which makes it much easier to accurately compare different codes. It proved more difficult to find parameters that gave reliable, reproducible dynamos steady in a drifting frame than had been anticipated, which accounts for the delay between inception and delivery. However, the benchmarks presented here have all now been checked to a surprisingly high

\* Corresponding author.

E-mail address: [cajones@maths.leeds.ac.uk](mailto:cajones@maths.leeds.ac.uk) (C.A. Jones).

level of accuracy by independently constructed codes, and they can all be computed to good accuracy without the need for excessively large computing resources. The teams contributing were generally using runs lasting a few days with typically between 32 and 128 processors in each run. Many such runs were performed while the benchmarks were established, but now that they have been fixed, reproducing these results will not be unduly expensive. During the course of this work, a number of issues arose which need particular care, and which had not previously been given much attention. We report on these below.

The objective here is to provide solutions which can be relatively easily verified rather than to provide a realistic model of either a giant planet interior or a stellar convection zone. Thus simple boundary conditions are used, and relatively low Rayleigh numbers are involved. This means that the diffusivities used are much larger than those in either giant planets or stars. In consequence, the heat flux coming out of the models is very much larger than that coming out of any realistic giant planet. Furthermore, the impenetrable boundaries are not a particularly realistic representation of giant planet or stellar convection zones. It is a task for future research to adapt the models to more physically realistic problems. Nevertheless, we have for definiteness adopted a well-defined model, based very crudely on Jupiter, as the basis of these benchmarks. Some codes use dimensionless parameters, and others a dimensional representation. While in principle it is simple to convert between these two, in practice it is easy to make errors, so we here report all the results in both dimensional and dimensionless form, to avoid any time-wasting confusion for those writing new codes.

In addition to the steady benchmarks, we also computed an unsteady dynamo benchmark case, which has ‘chaotic’ time-dependence. Only time-averages can be compared in this case, but it does test the heat transport terms more thoroughly. In steady benchmarks, most of the heat is transported by diffusion rather than convection, whereas in our unsteady case, the convective heat flux is greater than the diffusive heat flux.

Four codes took part in this benchmark exercise. The Leeds code and the MAGIC code are both adaptations of Boussinesq codes, and used the Lantz–Braginsky–Roberts (LBR) formulation of the anelastic approximation, described below. The ASH code (Anelastic Spherical Harmonic code) computes the pressure and density perturbations explicitly (see Clune et al., 1999). The Glatzmaier code comes in two versions, an older version which, like ASH, computes pressure and density perturbations explicitly, and a newer version based on the LBR formulation. Both versions of the Glatzmaier code gave the same results, to many significant figures of accuracy. These codes are all spectral, that is they all use a spherical harmonic expansion to represent the latitudinal and longitudinal dependence, and they use a toroidal–poloidal expansion to represent vector fields. The radial dependence can be represented either by finite differences or Chebyshev expansions. The ASH, MAGIC and Glatzmaier codes employ the same basic numerical methods because the ASH and MAGIC codes were derived from the original version of the Glatzmaier code (Glatzmaier, 1984). However, all three codes have been independently modified and parallelized since then. The Leeds code was developed independently and employs a somewhat different numerical solution method. Although no fully finite difference codes, or finite element codes, took part in this benchmark, it will be of interest to see results from such codes as they are developed.

## 2. Anelastic equations

We consider a spherical shell of gas, bounded by an inner spherical surface at  $r = r_i$  and an outer surface at  $r = r_o$ . The radius ratio

$\beta = r_i/r_o$ . Gravity acts radially inward. For simplicity, we assume that the bulk of the mass is concentrated inside the inner surface, and so gravity satisfies  $g = GM/r^2$ , with  $G$  being the gravitational constant and  $M$  the interior mass. The shell is rotating about the  $z$  axis with angular velocity  $\Omega$ , but the centrifugal acceleration is assumed negligible in comparison with gravity.

The anelastic equations were derived by Ogura and Phillips (1962) in the context of stably stratified atmospheres, and extended to convecting atmospheres by Gough (1969) and Gilman and Glatzmaier (1981). The approach used here follows Gilman and Glatzmaier (1981) and Lantz and Fan (1999). Further explanation of the anelastic equations is given in Miesch (2005). We first decompose the thermodynamic variables density, pressure and temperature into the sum of the basic state variables corresponding to the reference atmosphere (assumed close to adiabatic) denoted by an overbar, and a convective disturbance, denoted by a prime:

$$\rho = \bar{\rho} + \rho', \quad P = \bar{P} + p', \quad T = \bar{T} + T'. \quad (1)$$

The equation of motion for the velocity  $\mathbf{u}$  can then be written in the following dimensional form (see e.g. Chandrasekhar, 1961),

$$\frac{\partial \mathbf{u}}{\partial t} - \mathbf{u} \times \boldsymbol{\omega} = -\frac{\nabla p'}{\bar{\rho}} - \nabla \frac{1}{2} \mathbf{u}^2 + \frac{1}{\bar{\rho}} \mathbf{j} \times \mathbf{B} - 2\boldsymbol{\Omega} \times \mathbf{u} + \mathbf{F}_v + \frac{\rho' \mathbf{g}}{\bar{\rho}}, \quad (2)$$

$\mathbf{j} = (1/\mu)\nabla \times \mathbf{B}$  being the current density,  $\mathbf{B}$  the magnetic field and  $\mu$  the magnetic permeability of free space. The reference state variables satisfy the hydrostatic equation, which leads to a polytrope (see Section 3 below). We are neglecting centrifugal force in the reference state and its perturbation in Eq. (2). We assume constant kinematic viscosity  $\nu$ , and zero bulk viscosity, so that (Landau and Lifshitz, 1959, p. 48; Gilman and Glatzmaier, 1981; Eqs. (4)–(6)),

$$\mathbf{F}_v = \nu \left[ \frac{1}{\bar{\rho}} \frac{\partial}{\partial x_j} \bar{\rho} \left( \frac{\partial u_i}{\partial x_j} + \frac{\partial u_j}{\partial x_i} \right) - \frac{2}{3\bar{\rho}} \frac{\partial}{\partial x_i} \left( \bar{\rho} \frac{\partial u_j}{\partial x_j} \right) \right]. \quad (3)$$

A common alternative assumption is to take constant dynamic viscosity (see e.g. Glatzmaier and Gilman, 1981). Since it is natural to take the magnetic diffusivity as a constant independent of density, our choice of constant kinematic and thermal diffusivity has the convenience that the Prandtl numbers are also constant throughout the shell. The anelastic continuity equation is

$$\nabla \cdot \bar{\rho} \mathbf{u} = 0. \quad (4)$$

We assume a perfect gas,

$$P = \mathcal{R} \rho T, \quad (5)$$

and define the specific entropy  $S$  for the perfect gas (Landau and Lifshitz, 1959; p. 315) as

$$S = c_v \ln \frac{P}{\rho^\gamma} - S_0, \quad (6)$$

where  $\gamma = c_p/c_v$  and  $c_p$  and  $c_v$  are the specific heat capacities at constant pressure and volume, respectively, which we assume are constants. In all the benchmarks we consider here, the boundary condition that the entropy is held constant on the two spherical boundaries is applied. The constant in the definition of the entropy can therefore be conveniently chosen so that the entropy is zero on the outer boundary. Note that because the reference state is close to adiabatic, there is no need to introduce a separate perturbation entropy.

We write the dimensional form of the energy equation in terms of the entropy in order to eliminate the temperature completely from our formulation. This is possible if one chooses to represent the turbulent heat flux term as being proportional to the entropy gradient, as in ‘mixing length theory’. For turbulent flows the turbulent (eddy) thermal diffusivity is usually dominant and since

this acts through entropy diffusion rather than temperature diffusion, the energy flux down the gradient is  $-\kappa\bar{\rho}\bar{T}\nabla S$  (see e.g. Braginsky and Roberts, 1995), where  $\kappa$  is the turbulent thermal diffusivity, or entropy diffusivity, so

$$\bar{\rho}\bar{T}\left(\frac{\partial S}{\partial t} + (\mathbf{u} \cdot \nabla)S\right) = \nabla \cdot \kappa\bar{\rho}\bar{T}\nabla S + Q_v + Q_j, \quad (7)$$

with

$$Q_v = \sigma_{ij} \frac{\partial u_i}{\partial x_j}, \quad \sigma_{ij} = v\bar{\rho}\left(\frac{\partial u_i}{\partial x_j} + \frac{\partial u_j}{\partial x_i} - \frac{2}{3}\delta_{ij}\nabla \cdot \mathbf{u}\right), \quad Q_j = \eta\mu\mathbf{j}^2, \quad (8)$$

where  $\bar{T}$  is the basic state temperature,  $\kappa$  is the entropy diffusivity, assumed constant across shell, and  $Q_v$  and  $Q_j$  are respectively the viscous and Joule heating.

The induction and magnetic flux conservation equations are

$$\frac{\partial \mathbf{B}}{\partial t} = \nabla \times (\mathbf{u} \times \mathbf{B}) + \eta\nabla^2 \mathbf{B}, \quad \nabla \cdot \mathbf{B} = 0, \quad (9)$$

where  $\eta$  is the magnetic diffusivity, again assumed constant throughout the shell.

### 2.1. Boundary conditions

The entropy is fixed on the boundaries at  $r = r_i$  and  $r = r_o$ , so we set

$$S = \Delta S \quad \text{on } r = r_i, \quad \text{and } S = 0 \quad \text{on } r = r_o. \quad (10)$$

We use stress-free, impenetrable boundary conditions

$$u_r = \frac{\partial}{\partial r}\left(\frac{\mathbf{u}_\theta}{r}\right) = \frac{\partial}{\partial r}\left(\frac{\mathbf{u}_\phi}{r}\right) = 0, \quad \text{on } r = r_i \quad \text{and } r = r_o. \quad (11)$$

The material outside the shell (i.e. above the outer boundary and below the inner boundary) is assumed to be electrically insulating, again for simplicity. The magnetic field both below  $r_i$  and above  $r_o$  is therefore a potential magnetic field with no external or internal sources, which has to be finite at  $r = 0$  and decaying as  $r \rightarrow \infty$ . The boundary conditions for the spherical shell are that the magnetic field in the shell matches onto these potential fields, and these conditions can very easily be implemented for a spectral code. If the magnetic field in the shell is expanded in toroidal and poloidal scalars,

$$\mathbf{B} = \nabla \times \mathcal{T}\mathbf{r} + \nabla \times \nabla \times \mathcal{P}\mathbf{r}, \quad (12)$$

and  $\mathcal{T}$  and  $\mathcal{P}$  are expanded in spherical harmonics

$$\begin{aligned} \mathcal{T} &= \sum_{l=1}^{\infty} \sum_{m=-l}^{m=l} \mathcal{T}_{lm}(r) P_l^{|m|}(\cos \theta) e^{im\phi}, \\ \mathcal{P} &= \sum_{l=1}^{\infty} \sum_{m=-l}^{m=l} \mathcal{P}_{lm}(r) P_l^{|m|}(\cos \theta) e^{im\phi}, \end{aligned} \quad (13)$$

then at the inner and outer boundaries the field matches onto potential fields inside and outside the shell (see e.g. Roberts, 2007) to give

$$\begin{aligned} \mathcal{T}_{lm} = 0 \quad \text{on } r = r_i, r_o, \quad \frac{\partial \mathcal{P}_{lm}}{\partial r} - l \frac{\mathcal{P}_{lm}}{r} = 0 \quad \text{on } r = r_i \\ \text{and } \frac{\partial \mathcal{P}_{lm}}{\partial r} + (l+1) \frac{\mathcal{P}_{lm}}{r} = 0 \quad \text{on } r = r_o. \end{aligned} \quad (14)$$

For other codes, the Laplace equation for the magnetic field may need to be solved numerically in the insulating regions, though integral approaches (e.g. Iskakov and Dormy, 2005) may also be possible.

The choice of stress-free boundaries is motivated by the fact that more applications for anelastic codes are likely to require stress-free rather than no-slip boundaries, but stress-free (and electrically insulating) conditions mean that total angular momentum is conserved (see Appendix A), which can cause numerical difficulties (see Section 8).

### 2.2. Lantz–Braginsky–Roberts approximation

Lantz (1992) and Braginsky and Roberts (1995) independently noted that if the basic reference state is close to adiabatic, then the equation of motion (2) can be written in a form in which the only thermodynamic variable multiplying gravitational acceleration is the entropy

$$\frac{\partial \mathbf{u}}{\partial t} = \mathbf{u} \times \boldsymbol{\omega} - 2\boldsymbol{\Omega} \times \mathbf{u} + \frac{1}{\bar{\rho}} \mathbf{j} \times \mathbf{B} - \nabla \left( \frac{p'}{\bar{\rho}} + \frac{1}{2} \mathbf{u}^2 \right) + \mathbf{F}_v - \mathbf{g} \frac{S}{c_p} \quad (15)$$

where  $\boldsymbol{\omega}$  is the vorticity. Here we have assumed thermodynamic linearisation, that is the convective disturbances in (1) are small compared to their reference state values, and the specific entropy and equation of state are also linearised as in (17) below. The gradient of the gravitational potential perturbation, which would normally appear in Eq. (15), vanishes in our chosen benchmark problems because we are assuming the bulk of the mass is concentrated inside the inner boundary.

The significant difference between Eq. (15) and the more general compressible equation of motion (2) is that use has been made of the relation

$$\begin{aligned} -\frac{1}{\bar{\rho}} \nabla p' + \mathbf{g} \frac{\rho'}{\bar{\rho}} &= -\nabla \left( \frac{p'}{\bar{\rho}} \right) - \mathbf{g} \frac{S}{c_p} + \frac{p'}{\bar{\rho}} \left\{ \frac{1}{\gamma \bar{P}} \frac{d\bar{P}}{dr} - \frac{1}{\bar{\rho}} \frac{d\bar{\rho}}{dr} \right\} \hat{\mathbf{r}} \\ &\approx -\nabla \left( \frac{p'}{\bar{\rho}} \right) - \mathbf{g} \frac{S}{c_p}, \end{aligned} \quad (16)$$

see e.g. Section 4.2 of Braginsky and Roberts (1995). The omitted term in (16) is small compared with the others provided the reference atmosphere is close to adiabatic. This will be the case provided the dimensionless quantity  $\Delta S/c_p \ll 1$ , which is the fundamental assumption behind anelastic theory (Ogura and Phillips, 1962).

There are a number of ways of deriving the anelastic approximation (see e.g. Gilman and Glatzmaier, 1981; Gough, 1969; Lantz and Fan, 1999), but for this work we start from the assumption that  $\Delta S/c_p = \epsilon \ll 1$ . In this case, all the thermodynamic fluctuations from the reference state can be consistently taken as  $O(\epsilon)$  compared to their reference state values, that is  $\rho'/\bar{\rho}$ ,  $p'/\bar{P}$  and  $T'/\bar{T}$  are all  $O(\epsilon)$ . This then implies from the equation of motion that  $\mathbf{u}^2/c^2$  is  $O(\epsilon)$ ,  $c$  being the sound speed. If the length-scale is  $d = r_o - r_i$ , the timescale on which the convection evolves is then  $O(d/|\mathbf{u}|)$ , which is  $O(\epsilon^{-1/2})$  times longer than the free-fall time  $(d/g)^{1/2}$ . The time-derivative term in the mass conservation equation is then  $O(\epsilon)$  smaller than the retained terms in (4), so that a consistent anelastic system is derived by keeping only the leading order terms in  $\epsilon$ . For consistency, the magnetic field must have an Alfvén speed  $v_A$  which is small compared to the sound speed, in fact  $v_A^2/c^2 \sim O(\epsilon)$ . Since the fluctuations to the density, pressure and temperature are all  $O(\epsilon)$  compared to their reference state values, it follows that any changes to these quantities resulting from the convection itself are negligible. We therefore take the reference state variables  $\bar{\rho}$ ,  $\bar{P}$  and  $\bar{T}$  as fixed in time. The only exception to this rule is the entropy. Because the reference state entropy and the entropy fluctuations have the same order of magnitude,  $O(\Delta S)$ , the spherically averaged entropy profile can vary significantly with time, and forms part of the solution. It also follows that the Lantz–Braginsky–Roberts approximation is not an additional approximation to the anelastic approximation, but is a consequence of consistently ignoring all terms that are  $O(\epsilon)$  smaller than the leading order terms. Our approach has the merit that it is a mathematically well-defined asymptotic limit of the full system of equations. The question of whether the anelastic approximation is a satisfactory one to make in any specific physical application is of course an entirely different issue, and one that needs to be justified in each individual case.

When the thermodynamic fluctuations are taken as small perturbations from their reference state values, the entropy definition and the equation of state become

$$S = \frac{c_p}{\gamma} \left( \frac{p'}{\bar{p}} - \gamma \frac{\rho'}{\bar{\rho}} \right), \quad \frac{p'}{\bar{p}} = \frac{\rho'}{\bar{\rho}} + \frac{T'}{\bar{T}} \quad (17)$$

and if the equations are formulated in a way that computes the pressure, density and temperature perturbations explicitly, these forms of the entropy definition and equation of state must be used in place of (6) and (5), as these have been used to obtain (16). With formulations, such as the ASH code, which do compute pressure, density and temperature fluctuations explicitly, and work in dimensional variables, there is a scaling test which can be performed to check that all terms of order  $O(\epsilon^2)$  have been removed, described in Section 4.6 below. Such terms can be introduced by, for example, taking the acceleration term in the form  $(\bar{\rho} + \rho')\partial\mathbf{u}/\partial t$  rather than  $\bar{\rho}\partial\mathbf{u}/\partial t$ . Since the additional term  $\rho'\partial\mathbf{u}/\partial t$  vanishes in the anelastic limit, its introduction would make no difference in the limit  $\Delta S/c_p \rightarrow 0$ , but in the benchmarks a small but finite value of  $\Delta S/c_p$  is used, so to get precise agreement the  $O(\epsilon^2)$  terms must be consistently removed.

We note that not all formulations of the anelastic approximation are identical. Perhaps the only universal rule is that the mass-conservation equation always takes the form (4) in any formulation of the anelastic equations. Some authors (e.g. Gough, 1969; Miesch et al., 2000) allow the reference state to vary with time, on the grounds that while these variations are of the same order in  $\epsilon$  as the omitted  $\partial\mathbf{u}/\partial t$  term in (4), in specific physical situations they could be more physically significant. We also note that our formulation is restricted to the case where boundary conditions on the entropy are imposed. If it is required to apply boundary conditions on other thermodynamic variables, they must be computed explicitly (see e.g. Clune et al., 1999).

### 3. Polytopic reference state and the dimensionless formulation

With our assumption of gravity proportional to  $1/r^2$ , the anelastic equations admit an equilibrium polytopic solution,

$$\bar{\rho} = \rho_c \zeta^n, \quad \bar{T} = T_c \zeta, \quad \bar{p} = P_c \zeta^{n+1}, \quad \zeta = c_0 + \frac{c_1 d}{r}, \quad (18)$$

where  $n$  is the polytopic index,  $\zeta_i$  and  $\zeta_o$  are the values of  $\zeta$  at the inner and outer boundaries respectively,  $d = r_o - r_i$ , and the constants  $c_0$  and  $c_1$  are defined by

$$c_0 = \frac{2\zeta_o - \beta - 1}{1 - \beta}, \quad c_1 = \frac{(1 + \beta)(1 - \zeta_o)}{(1 - \beta)^2},$$

$$\zeta_o = \frac{\beta + 1}{\beta \exp(N_\rho/n) + 1}, \quad \zeta_i = \frac{1 + \beta - \zeta_o}{\beta}, \quad (19)$$

where  $N_\rho$  is the number of scale heights of density within the layer, that is  $N_\rho = \ln(\rho_i/\rho_o)$ , where  $\rho_i$  and  $\rho_o$  are the reference state densities at the inner and outer boundaries respectively. The values  $\rho_c$ ,  $p_c$  and  $T_c$  are the reference state density, pressure and temperature midway between the inner and outer surfaces of the shell. For a perfect gas close to adiabatic, the specific heats  $c_p = (n + 1)\mathcal{R}$ ,  $c_v = n\mathcal{R}$  and their ratio  $\gamma = (n + 1)/n$ ,  $\mathcal{R}$  being the gas constant. From the hydrostatic equation and the gas law it follows that  $c_1 = GM/c_p T_c d$ .

Some codes use dimensional equations, and some adopt a dimensionless formulation. The equations can be non-dimensionalised using the following units,

$$\text{length} : d, \quad \text{mass} : \rho_c d^3, \quad t = \frac{d^2}{\eta} t^*, \quad \mathbf{u} = \frac{\eta}{d} \mathbf{u}^*,$$

$$\nabla = \frac{1}{d} \nabla^*, \quad \rho = \rho_c \rho^*, \quad r = dr^*, \quad p = \Omega \rho_c \eta p^*,$$

$$\mathbf{B} = \sqrt{\Omega \rho_c \mu \eta} \mathbf{B}^*, \quad \mathbf{F}_v = \frac{\eta \eta}{d^3} \mathbf{F}_v^*, \quad S = \Delta S S^*, \quad T = T_c T^* \quad (20)$$

where  $\rho_c$  is density at  $\zeta = 1$  and  $\Delta S$  is the unit of entropy. The starred \* quantities in (21) represent dimensionless variables. In purely hydrodynamic computations, the timescale is taken as  $d^2/\nu$ . The quantities used to define the dimensionless variables can be combined to define the following dimensionless numbers

$$Ra = \frac{GMd\Delta S}{\nu \kappa c_p}, \quad Pr = \frac{\nu}{\kappa}, \quad Pm = \frac{\nu}{\eta}, \quad E = \frac{\nu}{\Omega d^2},$$

$$N_\rho = \ln\left(\frac{\rho_i}{\rho_o}\right), \quad n, \quad \beta = \frac{r_i}{r_o}, \quad (21)$$

where  $Ra$  is the Rayleigh number,  $Pr$  and  $Pm$  are the fluid and magnetic Prandtl numbers,  $E$  is the Ekman number,  $\exp(N_\rho)$  is the density ratio across the layer,  $n$  is the polytopic index and  $\beta$  is the radius ratio. After substituting (21) into (15) and dropping the star superscript \* we obtain

$$\frac{\partial \mathbf{u}}{\partial t} + \boldsymbol{\omega} \times \mathbf{u} = -\nabla \left( \frac{Pm}{E} \frac{p'}{\zeta^n} + \frac{1}{2} \mathbf{u}^2 \right)$$

$$+ Pm \left[ -\frac{2}{E} \hat{\mathbf{z}} \cdot \mathbf{u} + \frac{1}{E \zeta^n} (\nabla \times \mathbf{B}) \times \mathbf{B} + \mathbf{F}_v + \frac{Pm Ra}{Pr} \frac{S}{r^2} \hat{\mathbf{r}} \right] \quad (22)$$

where

$$\boldsymbol{\omega} = \nabla \times \mathbf{u}, \quad \mathbf{F}_v = \zeta^{-n} \frac{\partial}{\partial x_j} \zeta^n \left( \frac{\partial u_i}{\partial x_j} + \frac{\partial u_j}{\partial x_i} \right) - \frac{2}{3} \zeta^{-n} \frac{\partial}{\partial x_i} \zeta^n \frac{\partial u_j}{\partial x_j}. \quad (23)$$

The dimensionless entropy equation becomes

$$\frac{DS}{Dt} = \frac{Pm}{Pr} \zeta^{-n-1} \nabla \cdot \zeta^{n+1} \nabla S + \frac{Di}{\zeta} \left[ E^{-1} \zeta^{-n} (\nabla \times \mathbf{B})^2 + Q_v \right] \quad (24)$$

with the dissipation parameter  $Di$  defined as

$$Di = \frac{GM}{dT_c c_p} \frac{Pr}{Pm Ra} = \frac{c_1 Pr}{Pm Ra}, \quad Q_v = 2 \left[ e_{ij} e_{ij} - \frac{1}{3} (\nabla \cdot \mathbf{u})^2 \right],$$

$$e_{ij} = \frac{1}{2} \left( \frac{\partial u_i}{\partial x_j} + \frac{\partial u_j}{\partial x_i} \right). \quad (25)$$

The dimensionless induction equation is then

$$\frac{\partial \mathbf{B}}{\partial t} = \nabla \times (\mathbf{u} \times \mathbf{B}) + \nabla^2 \mathbf{B}. \quad (26)$$

### 4. Benchmark definitions and outputs

Since some codes use a dimensional formulation and others use a dimensionless formulation, we adopted a specific set of physical values to define the benchmarks, to facilitate comparisons between different codes. We also specify how the dimensional and dimensionless values are related, and in our tables of results we give both the dimensionless and dimensional values, to avoid confusion.

The defining physical inputs for all the models are the radius of the planet, the angular velocity, the mass, the density on the inner boundary and the gravitational constant  $G$ . The mean molecular weight was chosen so that the gas constant  $\mathcal{R} = 3.503 \times 10^7 \text{ erg g}^{-1} \text{ K}^{-1} = 3.503 \times 10^3 \text{ J kg}^{-1} \text{ K}^{-1}$ , approximately that for a giant planet. The radius ratio then gives the radius of the inner sphere, and hence the gap width, which is taken as the unit of length. The remaining six dimensionless parameters in (21) then specify the model completely. The Ekman number and the rotation rate determine the kinematic viscosity, and the Prandtl number then gives the thermal diffusivity, and the magnetic Prandtl number determines the magnetic diffusivity. The magnetic diffusivity is used to define the unit of time in dimensionless equations. Once the polytopic constants are evaluated from our dimensionless parameter choice using (19), the value of the density at the inner radius then determines the value of  $\rho_c$  in the polytopic law

$\rho = \rho_c \zeta^n$ , thus determining the density at the outer radius. The pressure  $p_c$  that appears in the polytropic law  $p = p_c \zeta^{n+1}$  satisfies  $p_c = GM\rho_c/(n+1)c_1d$  and so is now determined. From  $p_c$  we can compute the pressure on the inner and outer boundaries in the reference state. Next the equation of state determines the temperatures at the boundaries, and the polytropic index gives  $c_p = (n+1)\mathcal{R}$ . Finally, the chosen Rayleigh number determines the entropy jump across the shell  $\Delta S = \text{Rav}\kappa c_p / GMd$ . The unit of energy is then  $\rho_c \eta^2 d$ , and of energy density is  $\rho_c \eta^2 / d^2$ . In hydrodynamic cases, we set  $\eta = v$ , so the energy unit is then also  $\rho_c v^2 d$ .

The unit of total luminosity comes from the conducted heat flux,  $\mathbf{F} = -\kappa \rho T \nabla S$  erg  $\text{cm}^{-2} \text{s}^{-1}$ . The unit of  $\rho$  is  $\rho_c$ , the unit of  $T$  is  $T_c$ , the unit of specific entropy is  $\Delta S$  and the unit of distance is  $d$ , so the unit of heat flux is  $\kappa \rho_c T_c \Delta S / d$  erg  $\text{cm}^{-2} \text{s}^{-1}$ , and the unit of luminosity is  $\kappa \rho_c T_c \Delta S d$  erg  $\text{s}^{-1}$ .

The unit of magnetic field is  $\sqrt{\Omega \rho_c \mu \eta}$ . If SI units are used for these quantities,  $\mu = 4\pi \times 10^{-7}$  and the resulting field is in Tesla. If cgs units are used, current density is defined as  $(c/4\pi) \nabla \times \mathbf{B}$ , and  $\mathbf{B}$  is then in gauss, 1 T being  $10^4$  G. In cgs units,  $\mu$  is taken as 1, and the Lorentz force is then  $(1/c) \mathbf{j} \times \mathbf{B}$ .

All these quantities are given below in Tables 1, 3 and 5. The outputs requested from the participating partners for the two benchmarks which are steady in a drifting frame were various components of the energy, the luminosity, the drift rate and point values of some quantities in the equatorial plane.

#### 4.1. Energies

The kinetic energy is defined as

$$KE = \int_V \frac{1}{2} \bar{\rho} \mathbf{u}^2 r^2 \sin \theta dr d\theta d\phi, \quad (27)$$

in spherical polar coordinates  $(r, \theta, \phi)$ , the volume integral being over the whole spherical shell. Note that  $\bar{\rho}$  is a function of  $r$  in this anelastic case, unlike the Boussinesq case. We also give the kinetic energy density, which is  $KE$  divided by the volume  $V$  of the shell. The shell volume  $V$  in dimensionless units is

$$V = \frac{4\pi}{3} \left( \frac{1}{(1-\beta)^3} - \frac{\beta^3}{(1-\beta)^3} \right), \quad (28)$$

and the physical volume is  $Vd^3$ .

The magnetic energy is defined as the magnetic energy inside the fluid. The energy of the potential fields both inside and outside the shell are not included in this definition, so

$$ME = \int_V \frac{1}{2\mu} \mathbf{B}^2 r^2 \sin \theta dr d\theta d\phi. \quad (29)$$

The kinetic energy of the differential rotation and the meridional circulation are also quantities of interest. We define the azimuthal average by

$$\langle \mathbf{u} \rangle = \frac{1}{2\pi} \int_0^{2\pi} \mathbf{u} d\phi. \quad (30)$$

The kinetic energy of the zonal flow, or differential rotation, is then

$$KE_{zonal} = \int_V \frac{1}{2} \bar{\rho} \langle u_\phi \rangle^2 r^2 \sin \theta dr d\theta d\phi, \quad (31)$$

the integral being over the whole spherical shell  $V$ . The kinetic energy of the meridional flow is then

$$KE_{meridional} = \int_V \frac{1}{2} \bar{\rho} \left( \langle u_r \rangle^2 + \langle u_\theta \rangle^2 \right) r^2 \sin \theta dr d\theta d\phi. \quad (32)$$

In rapidly rotating flows, the meridional kinetic energy is usually much smaller than the zonal kinetic energy. The magnetic energy can be decomposed similarly,

$$ME_{zonal} = \int_V \frac{1}{2\mu} \langle B_\phi \rangle^2 r^2 \sin \theta dr d\theta d\phi, \quad (33)$$

and

$$ME_{meridional} = \int_V \frac{1}{2\mu} \left( \langle B_r \rangle^2 + \langle B_\theta \rangle^2 \right) r^2 \sin \theta dr d\theta d\phi. \quad (34)$$

#### 4.2. Luminosity

The luminosity is

$$L = \int_s -\kappa \bar{\rho} T \frac{\partial S}{\partial r} r^2 \sin \theta d\theta d\phi, \quad (35)$$

where the integral is taken over the top surface or the bottom surface. These quantities have the same magnitude in a steady state solution (or steady drifting solution) because there are no internal heat sources. Note that viscous and ohmic heating are not internal heat sources, but are balanced by the work done against gravity by the buoyant convection in the overall energy balance. The luminosity coming from the conduction state, when no convection occurs, is given by (35) with the conduction state entropy  $S_{cond}$  defined by

$$S_{cond} = \frac{\Delta S (\zeta_o^{-n} - \zeta_i^{-n})}{\zeta_o^{-n} - \zeta_i^{-n}}. \quad (36)$$

This gives the basic state luminosity as  $4\pi n c_1 \zeta_i^n (\exp N_\rho - 1)^{-1}$  times the unit of luminosity. This value is given for each benchmark in Tables 1, 3 and 5. The Nusselt number is defined as the actual output luminosity divided by this basic state luminosity.

All the models reported that for the benchmarks steady in the drifting frame, the luminosity evaluated at the top and bottom eventually became the same, so only the one value is recorded here. Since the Nusselt number can easily be obtained by dividing by the basic state heat flux listed in the defining tables, this is not given separately. For the unsteady benchmark, the top and bottom luminosities are not the same at any one instant, though their long term averages must converge to the same value.

#### 4.3. Drift speed

In some parameter regimes, solutions that are steady in a drifting frame can be found with a uniform angular velocity,  $\omega$ . If the solution is written as  $f(r, \theta, \phi - \omega t)$  then if the solution has  $m$ -fold symmetry the period  $\tau$  is related to the angular drift frequency by  $\omega = 2\pi/m\tau$ . In dimensionless units  $\omega = \omega_d \eta / d^2$  and the unit of  $\tau$  is  $d^2/\eta$ . The drift speed can easily be expressed as a fraction of the angular rotation velocity using the formula  $\omega/\Omega = \omega_d E / Pm$ . The drift angular speed in compressible rotating convection is typically significantly faster than in the Boussinesq case (Jones et al., 2009). In the steady benchmark Tables 2 and 4 both the period and angular speeds are quoted.

#### 4.4. Point values

For the Boussinesq benchmark (Christensen et al., 2001) contributors were requested to supply data values at specific points in the solution. We adopt here the same principle for the two benchmarks that are steady in a drifting frame. We define the specific points as having a radial location midway between the inner and outer shells,  $r_m = (r_i + r_o)/2$ , and lying in the equatorial plane,  $\theta = \pi/2$ . Since the solution drifts in longitude, no fixed point can

be taken, but instead we choose the longitude at which the radial velocity  $u_r$  is zero at  $r_m$  and  $\theta = \pi/2$ . We select the point at which  $u_r$  is increasing with longitude rather than decreasing with longitude,  $\partial u_r / \partial \phi > 0$ . For both our steady benchmarks this is sufficient to determine the specified point. Because our solutions have azimuthal symmetry of order  $m$ , there are  $m$  equivalent points, but all the data are identical at all equivalent points, so the values are well-defined. We give the azimuthal velocity  $u_\phi$ , the entropy  $S$  and the latitudinal component of magnetic field  $B_\theta$  in the steady dynamo benchmark case. Since the field in this dynamo has dipolar parity,  $B_r = B_\phi = 0$  on the equatorial plane, so only  $B_\theta$  is appropriate here. The dynamo equations are invariant under a reversal of the sign of the magnetic field, so  $B_\theta$  can have positive or negative values at the critical point, depending on the dipole polarity found, which is determined by the initial condition. For the unsteady benchmark, the point values vary with time, so we do not record these values.

#### 4.5. Resolution

All the codes that contributed to the benchmark were pseudo-spectral, that is the  $\theta$  and  $\phi$  dependence was represented by an expansion in spherical harmonics. The spherical harmonic expansion of the dependent variables is truncated, and nonlinear terms are evaluated by transforming to a mesh in physical space. This mesh has typically more points than the truncation level of the spherical harmonic expansion, typically in the  $\theta$  direction 50% more points than harmonics. In the  $\phi$  direction, there are typically three times as many points on the physical mesh as the order of the highest harmonic, as the  $m$  in the expansion can take positive or negative values. The resolution values shown in Tables 2, 4 and 6 refer to the number of points on the physical mesh used, so these are typically larger than the order or degree of the highest spherical harmonic used.

The codes differed in the treatment of the radial equation. Some used expansion in Chebyshev polynomials, others used high order finite differences. The radial resolution  $N_r$  quoted in the tables can therefore either be the number of grid points in  $r$  or the number of Chebyshev polynomials used. So a quoted resolution of  $N_r \times N_\theta \times N_\phi$  means  $N_r$  points or polynomials in the radial direction,  $N_\theta$  latitudinal points on the physical space grid and  $N_\phi$  longitudinal points on the physical space grid. We also quote the timestep used in the simulations and the length of the run. The timestep required is of course dependent on the details of the numerical method, but the information is included to help researchers to estimate the computational resources needed to tackle anelastic convection problems.

#### 4.6. Scaling test

Formulations in dimensional variables will require an input value of  $\Delta S$  and one might wonder whether the solution should depend on the dimensionless parameter  $\Delta S/c_p$  as well as the values of the dimensionless parameters (21). If the rotation rate and all the diffusivities are halved, then provided the value of  $\Delta S$  is divided by four, and all other quantities left the same, all the dimensionless parameters are unchanged. The timescale changes by a factor 2, so the energies obtained should be exactly four times less than in the original benchmark, and the luminosity exactly eight times less. Note that the dimensional timestep should be doubled. So varying  $\Delta S/c_p$  and keeping the dimensionless parameters the same only scales the solution, so nothing is fundamentally changed. Because in the anelastic approximation this scaling changes  $\Delta S/c_p$ , this test will not be passed if there are terms of order  $(\Delta S/c_p)^2$  left in the formulation. If the equations are formulated in the dimensionless LBR form, this test is not necessary,

because only the dimensionless variables appear, and  $\Delta S/c_p$  is scaled out of the equations at the start. The ASH code, and the older version of the Glatzmaier code which did not use the LBR formulation, both passed this test.

### 5. Hydrodynamic benchmark

The dimensionless parameters for this run are specified in Table 1. They were chosen so that a solution that is steady in a drifting frame could be obtained, so that the kinetic energy, luminosity and drift speed all tend to well-defined constant values as the time integration proceeds. The value of  $N_\rho = 5$  gives a density ratio of nearly 150 across the shell, so compressible effects on the convection are very strong. Stress-free, constant entropy boundary conditions are applied.

A separate linear code for evaluating the Rayleigh number at the onset of convection (Jones et al., 2009) was used to determine the onset values for this hydrodynamic benchmark. Linear disturbances have azimuthal and time-dependence  $\sim \exp(im\phi - i\omega_m t)$ ,  $m$  being an integer. With Table 1 parameters  $N_\rho = 5$ ,  $n = 2$ ,  $r_i/r_o = 0.35$ ,  $Pr = 1$ ,  $E = 0.001$  and stress-free boundaries, the first mode to become unstable has an azimuthal wavenumber  $m = 20$ , and occurs at  $Ra_{crit} = 283175.01$ . The corresponding frequency is  $\omega_m = 269.56$ . In the nonlinear hydrodynamic benchmark simulations, the solution developing from the  $m = 19$  mode was generally found, and this is the benchmark solution. The onset for  $m = 19$  is very close to the  $m = 20$  onset, with parameters  $Ra = 283779.37$ ,  $m = 19$ ,  $\omega_m = 279.34$ . The conducted heat flux with no convection is 3.954041 in the dimensionless units. To help those developing codes, we also used the linear code to evaluate the growth rate and frequency of small disturbances to the basic reference state, that is the state defined by Eq. (18) and (36) at the benchmark value of the Rayleigh number. In dimensionless units, at the hydrodynamic benchmark parameter values listed in Table 1, the growth rate of  $m = 19$  small disturbances is 77.551 with frequency 269.05, using our linear code. In the dimensional units this growth rate corresponds to 1.1793 days<sup>-1</sup>. The energy of the disturbance, proportional to the square of the velocity perturbation, grows at twice this value, i.e. 2.3586 days<sup>-1</sup>. As part of our testing procedures, we computed the growth rate by observing the development of the energy of a small disturbance from the basic

**Table 1**

Parameters for the hydrodynamic benchmark. The chosen defining physical input values determine the conversion from dimensionless to dimensional units.

#### Dimensionless parameters

$$E = 10^{-3}, N_\rho = 5, \beta = 0.35, Ra = 351,806, Pr = 1, n = 2$$

#### Defining physical input values

$$r_o = 7 \times 10^9 \text{ cm}, \Omega = 1.76 \times 10^{-4} \text{ s}^{-1}, M = 1.9 \times 10^{30} \text{ g}, \rho_i = 1.1 \text{ g cm}^{-3}, \\ R = 3.503 \times 10^7 \text{ erg g}^{-1} \text{ K}^{-1}, G = 6.67 \times 10^{-8} \text{ g}^{-1} \text{ cm}^3 \text{ s}^{-2}$$

#### Polytropic constants

$$\zeta_0 = 0.256465, \zeta_i = 3.124385, c_0 = -1.287800, c_1 = 2.375792, V = 14.598801$$

#### Derived physical input values

$$r_i = 2.45 \times 10^9 \text{ cm}, d = 4.55 \times 10^9 \text{ cm}, v = 3.64364 \times 10^{12} \text{ cm}^2 \text{ s}^{-1}, \\ \kappa = 3.64364 \times 10^{12} \text{ cm}^2 \text{ s}^{-1}$$

#### Derived thermodynamic quantities in the model

$$\rho_c = 0.112684 \text{ g cm}^{-3}, \rho_o = 0.00741174 \text{ g cm}^{-3}, T_i = 348,548 \text{ K}, T_c = 111,557 \text{ K}, \\ T_o = 28,611 \text{ K},$$

$$p_i = 1.343061 \times 10^{13} \text{ dyne cm}^{-2}, p_c = 4.403540 \times 10^{11} \text{ dyne cm}^{-2}, \\ p_o = 7.428259 \times 10^9 \text{ dyne cm}^{-2},$$

$$\Delta S = 851225.7 \text{ erg g}^{-1} \text{ K}^{-1}, c_p = 1.0509 \times 10^8 \text{ erg g}^{-1} \text{ K}^{-1}, \Delta S/c_p = 0.0081, \\ \text{Basic state luminosity} = 7.014464 \times 10^{32} \text{ erg s}^{-1}$$

#### Dimensionless units

$$\text{Velocity } 800.8 \text{ cm s}^{-1}; \text{ time } 5.681818 \times 10^6 \text{ s}; \text{ distance } 4.55 \times 10^9 \text{ cm}; \\ \text{energy } 6.806845 \times 10^{33} \text{ erg}$$

$$\text{Energy density } 7.226228 \times 10^4 \text{ erg cm}^{-3}; \text{ luminosity } 1.773999 \times 10^{32} \text{ erg s}^{-1}$$

**Table 2**  
Results from the hydrodynamic benchmark.

Code	Leeds	Glatzmaier	ASH	MAGIC
K.E. (erg)	$5.57195 \times 10^{35}$	$5.57028 \times 10^{35}$	$5.52650 \times 10^{35}$	$5.57062 \times 10^{35}$
K.E. dimensionless	81.8581	81.8335	81.1903	81.8385
K.E. density (erg cm <sup>-3</sup> )	$4.05188 \times 10^5$	$4.05066 \times 10^5$	$4.01882 \times 10^5$	$4.05091 \times 10^5$
Luminosity (erg s <sup>-1</sup> )	$7.44878 \times 10^{32}$	$7.44878 \times 10^{32}$	$7.44877 \times 10^{32}$	$7.44880 \times 10^{32}$
Luminosity dimensionless	4.19886	4.19886	4.19886	4.19887
Zonal K.E. (erg)	$6.38294 \times 10^{34}$	$6.38099 \times 10^{34}$	$6.33063 \times 10^{34}$	$6.38151 \times 10^{34}$
Zonal K.E. dimensionless	9.37724	9.37437	9.30039	9.37514
Meridional K.E. (erg)	$1.49875 \times 10^{32}$	$1.49825 \times 10^{32}$	$1.48637 \times 10^{32}$	$1.49843 \times 10^{32}$
Meridional K.E. dimensionless	0.0220183	0.0220109	0.0218364	0.0220136
Period $\tau$ dimensional (days)	1.23264	1.23263	1.23263	1.23241
Period $\tau$ dimensionless	0.0187440	0.0187440	0.0187439	0.0187404
$\omega = 2\pi/19\tau$ (rad s <sup>-1</sup> )	$3.10511 \times 10^{-6}$	$3.10512 \times 10^{-6}$	$3.10512 \times 10^{-6}$	$3.10570 \times 10^{-6}$
$\omega = 2\pi/19\tau$ dimensionless	17.6427	17.6427	17.6428	17.6460
$u_\phi$ at $u_r = 0$ (cm s <sup>-1</sup> )	690.15	690.27	687.65	689.66
$u_\phi$ at $u_r = 0$ dimensionless	0.86183	0.86197	0.85871	0.86122
$S$ at $u_r = 0$ (erg g <sup>-1</sup> K <sup>-1</sup> )	$7.9420 \times 10^5$	$7.9452 \times 10^5$	$7.9766 \times 10^5$	$7.9452 \times 10^5$
$S$ at $u_r = 0$ dimensionless	0.93301	0.93338	0.93707	0.93338
Resolution	$128 \times 192 \times 384$	$121 \times 512 \times 1024$	$129 \times 256 \times 512$	$121 \times 192 \times 384$
Timestep (s)	14.2	33	33	28.41
Timestep dimensionless	$2.5 \times 10^{-6}$	$5.8 \times 10^{-6}$	$5.8 \times 10^{-6}$	$5 \times 10^{-6}$
Run length (days)	92	450	154.4	197.29
Run length dimensionless	1.4	6.8	2.35	3.0

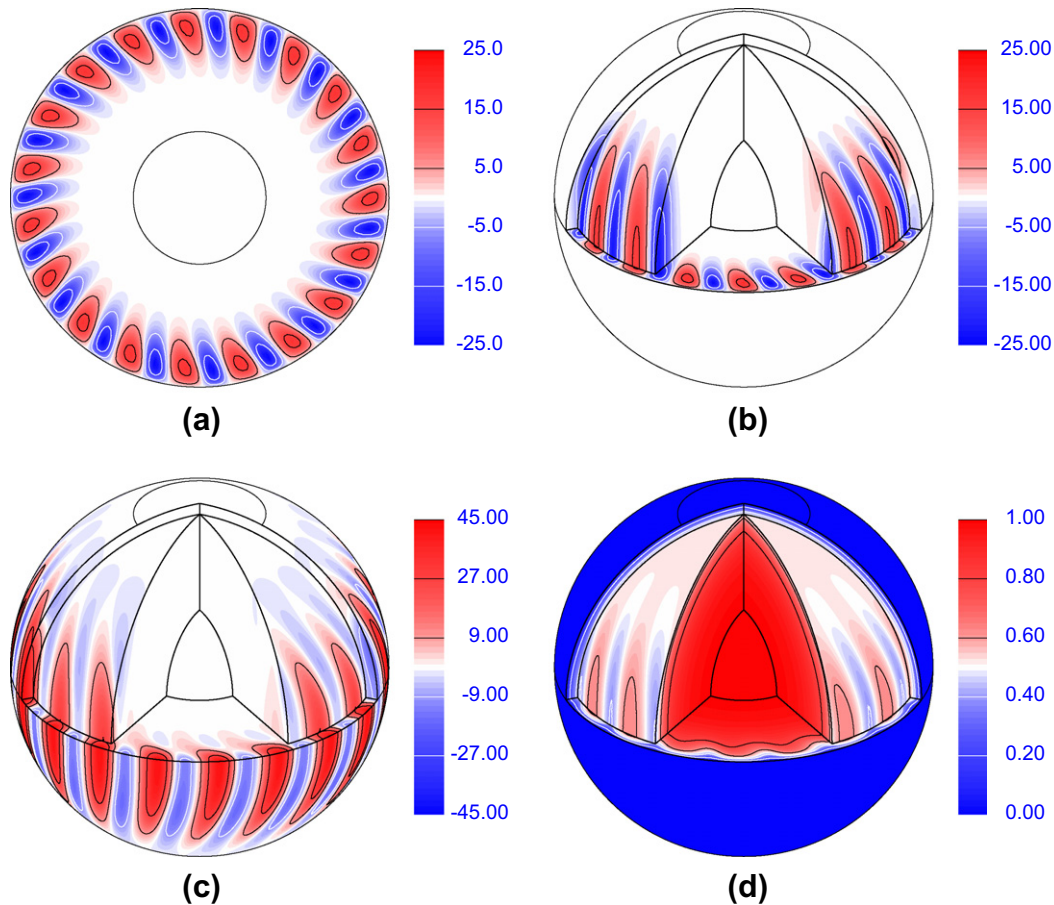


**Fig. 1.** Hydrodynamic benchmark. Dimensionless units throughout. (a) Radial velocity  $u_r$ , in the equatorial plane. The  $m = 19$  azimuthal symmetry is apparent. Black contours at  $u_r = 5$  and  $u_r = 15$ , white contours at  $u_r = -5$  and  $u_r = -15$ . (b) Cut-away plot of the radial velocity  $u_r$ , showing the columnar structure and the concentration of convection near the outer boundary. The innermost shell is the inner boundary at  $r = 0.538$ , the interior shell is at  $r = 1.437$ , and the outer shell is the outer boundary at  $r = 1.538$ . The latitudinal circle where the tangent cylinder, the imaginary cylinder with axis parallel to the rotation axis that touches the inner core, cuts the outer boundary is also shown. Contours as in (a). (c) The azimuthal velocity  $u_\phi$ . Again the columnar structure is evident, as is the preponderance of eastward to westward flow near the outer boundary. The stress-free boundary means  $u_\phi$  is non-zero on the displayed outer boundary. Black contours at  $u_\phi = 9$  and  $u_\phi = 27$ , white contour at  $u_\phi = -9$ . (d) The entropy  $S$ . The entropy gradient is strongest near the outer boundary. Note that the entropy in the interior is strongly correlated with  $u_r$ . White contours at  $S = 0.2, 0.4$ , black contours at  $S = 0.6, 0.8$ .

**Table 3**

Parameters for the steady dynamo benchmark.

<i>Dimensionless parameters</i>	
$E = 2 \times 10^{-3}$ , $N_\rho = 3$ , $\beta = 0.35$ , $Ra = 80,000$ , $Pr = 1$ , $Pm = 50$ , $n = 2$	
<i>Defining physical input values</i>	
$r_o = 7 \times 10^9$ cm, $\Omega = 1.76 \times 10^{-4}$ s $^{-1}$ , $M = 1.9 \times 10^{30}$ g, $\rho_i = 1.1$ g cm $^{-3}$ , $\mathcal{R} = 3.503 \times 10^7$ erg g $^{-1}$ K $^{-1}$ , $G = 6.67 \times 10^{-8}$ g $^{-1}$ cm $^3$ s $^{-2}$	
<i>Polytropic constants</i>	
$\zeta_0 = 0.525580$ , $\zeta_1 = 2.355486$ , $c_0 = -0.459754$ , $c_1 = 1.515898$ , $V = 14.598801$	
<i>Derived physical input values</i>	
$r_i = 2.45 \times 10^9$ cm, $d = 4.55 \times 10^9$ cm, $v = 7.28728 \times 10^{12}$ cm $^2$ s $^{-1}$ , $\kappa = 7.28728 \times 10^{12}$ cm $^2$ s $^{-1}$ , $\eta = 1.457456 \times 10^{11}$ cm $^2$ s $^{-1}$	
<i>Derived thermodynamic quantities in the model</i>	
$\rho_c = 0.198258$ g cm $^{-3}$ , $\rho_o = 0.0547658$ g cm $^{-3}$ , $T_i = 411,829$ K, $T_c = 174,838$ K, $T_o = 91891.5$ K, $p_i = 1.586901 \times 10^{13}$ dyne cm $^{-2}$ , $p_c = 1.214251 \times 10^{12}$ dyne cm $^{-2}$ , $p_o = 1.762888 \times 10^{11}$ dyne cm $^{-2}$ , $\Delta S = 774268.3$ erg g $^{-1}$ K $^{-1}$ , $c_p = 1.0509 \times 10^8$ erg g $^{-1}$ K $^{-1}$ , $\Delta S/c_p = 0.0074$ , Basic state luminosity = $9.856055 \times 10^{33}$ erg s $^{-1}$	
<i>Dimensionless units</i>	
Velocity $32.032$ cm s $^{-1}$ ; time $1.420455 \times 10^8$ s; distance $4.55 \times 10^9$ cm; energy $1.916170 \times 10^{31}$ erg; Energy density $203.4229$ erg cm $^{-3}$ ; luminosity $8.898904 \times 10^{32}$ erg s $^{-1}$ ; magnetic field $7994.197$ G	

reference state. The Leeds code gave  $2.3566$  days $^{-1}$  and the ASH code  $2.35654$  days $^{-1}$ , both in good agreement with the linear code.

A nonlinear solution at the parameters given in Table 1 was found with  $m = 19$  azimuthal symmetry and the results are shown in Table 2. The quantities displayed in Table 2 are those defined in Section 4. Although the solution can be obtained cheaply by assuming this azimuthal symmetry, this was not done in the sim-

ulations presented here. The codes all evolved naturally to the state with this symmetry, showing that it is a stable attractor, i.e. stable to small disturbances with any azimuthal symmetry. The  $m = 19$  solution is not unique; for example, an  $m = 20$  solution with a slightly lower kinetic energy than the  $m = 19$  case is also stable. The  $m = 19$  solution can conveniently be found if the initial condition is specified as a small  $m = 19$  entropy perturbation, with a smaller  $m = 1$  perturbation, which will allow all  $m$  modes to populate initially, all other variables being initially zero.

In Fig. 1 we display the characteristic properties of this hydrodynamic benchmark solution. The radial velocity plot in Fig. 1a makes the  $m = 19$  symmetry apparent. In Fig. 1b a cutaway section of the radial velocity is shown, and the proximity of the convection to the outer boundary is clear, though despite this the columnar structure of the convection is evident. The azimuthal velocity is shown in Fig. 1c. The stress-free boundary condition means  $u_\phi$  is non-zero at the outer boundary. Although the convective structure is still clear, the predominantly eastward (positive) flow is apparent. The entropy is shown in Fig. 1d. The basic state entropy gradient is strongest near the outer sphere, and this is why the convection is predominantly close to the outer sphere.

## 6. Steady dynamo benchmark

The dimensionless parameters for this run are specified in Table 3. As before we set the polytropic index  $n = 2$ . Again, stress-free, impenetrable, electrically insulating boundary conditions were applied, and the entropy set to  $\Delta S$  on the inner boundary and zero on the outer boundary. The solution sought is steady in a drifting frame, so that the computed magnetic and kinetic energies tend to time-independent well-defined values, greatly facilitating comparison between different codes.

**Table 4**

Results from the steady dynamo benchmark.

Code	Leeds	Glatzmaier	ASH	MAGIC
M.E. (erg)	$6.13528 \times 10^{36}$	$6.13333 \times 10^{36}$	$6.08670 \times 10^{36}$	$6.12692 \times 10^{36}$
M.E. dimensionless	$3.20185 \times 10^5$	$3.20083 \times 10^5$	$3.17649 \times 10^5$	$3.19748 \times 10^5$
M.E. density (erg cm $^{-3}$ )	$4.46152 \times 10^6$	$4.46010 \times 10^6$	$4.42619 \times 10^6$	$4.45544 \times 10^6$
K.E. (erg)	$8.03654 \times 10^{36}$	$8.03623 \times 10^{36}$	$7.97382 \times 10^{36}$	$8.03712 \times 10^{36}$
K.E. dimensionless	$4.19407 \times 10^5$	$4.19390 \times 10^5$	$4.16134 \times 10^5$	$4.19437 \times 10^5$
K.E. density (erg cm $^{-3}$ )	$5.84410 \times 10^6$	$5.84387 \times 10^6$	$5.79849 \times 10^6$	$5.84452 \times 10^6$
Luminosity (erg s $^{-1}$ )	$1.02364 \times 10^{34}$	$1.02364 \times 10^{34}$	$1.02364 \times 10^{34}$	$1.02363 \times 10^{34}$
Luminosity dimensionless	11.5030	11.5030	11.5030	11.5029
Zonal M.E. (erg)	$4.62190 \times 10^{36}$	$4.62046 \times 10^{36}$	$4.58531 \times 10^{36}$	$4.61589 \times 10^{36}$
Zonal M.E. dimensionless	$2.41205 \times 10^5$	$2.41130 \times 10^5$	$2.39295 \times 10^5$	$2.40891 \times 10^5$
Meridional M.E. (erg)	$3.25104 \times 10^{35}$	$3.24927 \times 10^{35}$	$3.22473 \times 10^{35}$	$3.24307 \times 10^{35}$
Meridional M.E. dimensionless	$1.69664 \times 10^4$	$1.69571 \times 10^4$	$1.68290 \times 10^4$	$1.69248 \times 10^4$
Zonal K.E. (erg)	$1.15305 \times 10^{36}$	$1.15318 \times 10^{36}$	$1.14414 \times 10^{36}$	$1.15435 \times 10^{36}$
Zonal K.E. dimensionless	$6.01749 \times 10^4$	$6.01815 \times 10^4$	$5.97098 \times 10^4$	$6.02426 \times 10^4$
Meridional K.E. (erg)	$1.01587 \times 10^{33}$	$1.01587 \times 10^{33}$	$1.00794 \times 10^{33}$	$1.01475 \times 10^{33}$
Meridional K.E. dimensionless	53.0157	53.0110	52.6019	52.9572
Period $\tau$ (days)	2.41180	2.41175	2.41175	2.41136
Period $\tau$ dimensionless	$1.46699 \times 10^{-3}$	$1.46696 \times 10^{-3}$	$1.46696 \times 10^{-3}$	$1.46672 \times 10^{-3}$
$\omega = 2\pi/7\tau$ (rad s $^{-1}$ )	$4.30752 \times 10^{-6}$	$4.30760 \times 10^{-6}$	$4.30761 \times 10^{-6}$	$4.30830 \times 10^{-6}$
$\omega = 2\pi/7\tau$ dimensionless	611.864	611.875	611.877	611.975
$u_\phi$ at $u_r = 0$ (cm s $^{-1}$ )	-2939.9	-2942.2	-2935.1	-2942.1
$u_\phi$ at $u_r = 0$ dimensionless	-91.780	-91.852	-91.631	-91.848
$S$ at $u_r = 0$ (erg g $^{-1}$ K $^{-1}$ )	$6.0893 \times 10^5$	$6.0893 \times 10^5$	$6.0889 \times 10^5$	$6.0892 \times 10^5$
$S$ at $u_r = 0$ dimensionless	0.78646	0.78646	0.78641	0.78645
$B_\theta$ at $u_r = 0$ (G)	$\pm 271.39$	$\pm 272.92$	$\pm 273.40$	$\pm 272.38$
$B_\theta$ at $u_r = 0$ dimensionless	$\pm 0.03395$	$\pm 0.03414$	$\pm 0.03420$	$\pm 0.03407$
Resolution	$128 \times 144 \times 252$	$65 \times 128 \times 256$	$129 \times 128 \times 256$	$65 \times 128 \times 256$
Timestep (s)	142	300	200	142.05
Timestep dimensionless	$10^{-6}$	$2.1 \times 10^{-6}$	$1.4 \times 10^{-6}$	$10^{-6}$
Run length (days)	8648	17,000	6673	9173.77
Run length dimensionless	5.26	10.3	4.06	5.58

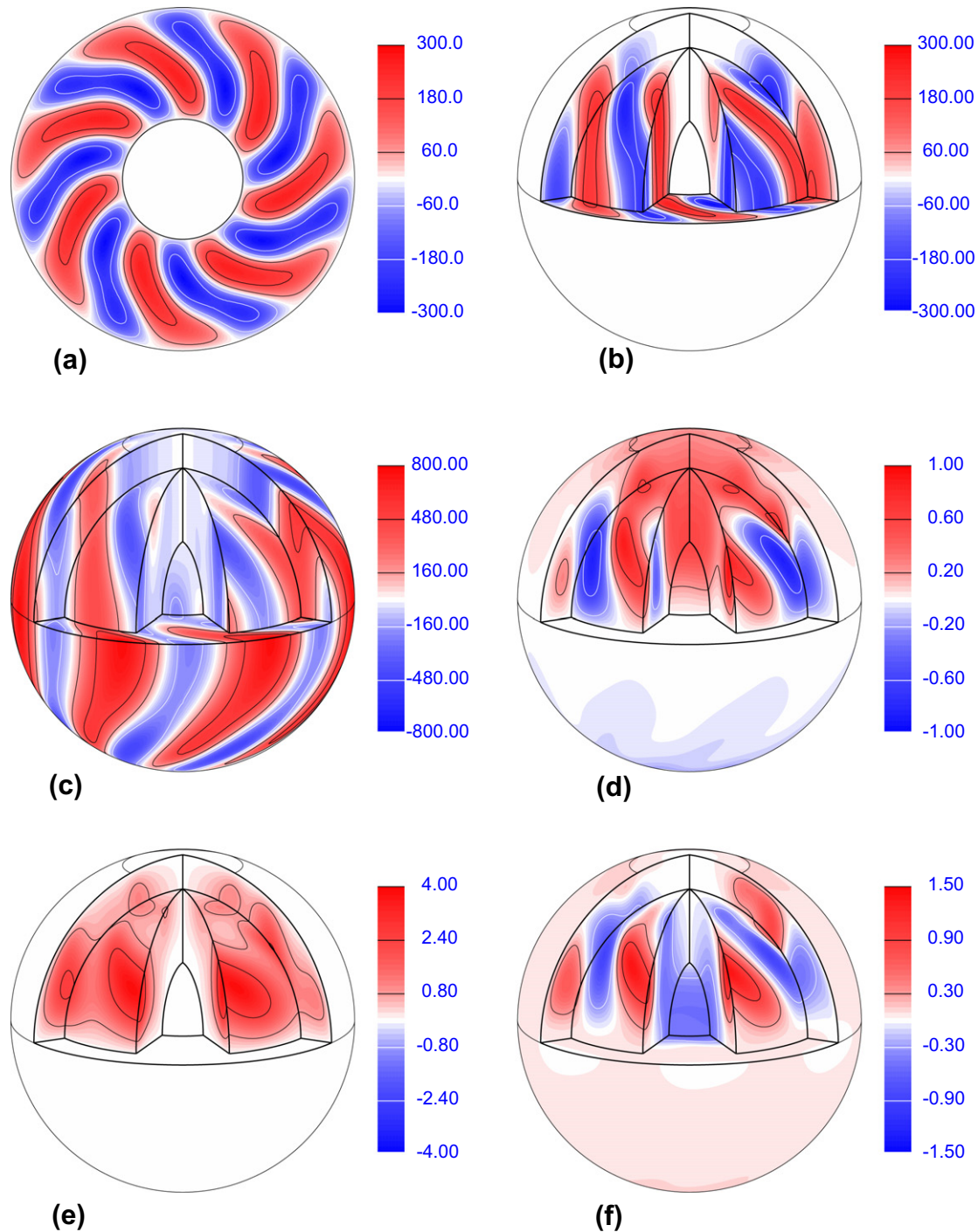


**Fig. 2.** Steady dynamo benchmark. Dimensionless units throughout. (a) Radial velocity in the equatorial plane. The  $m = 7$  azimuthal symmetry is apparent. Black contours at  $u_r = 60$  and  $u_r = 180$ , white contours at  $u_r = -60$  and  $u_r = -180$ . (b) Cut-away plot of the radial velocity. Note that flow is columnar, that is only weakly  $z$ -dependent.  $u_r$  is symmetric about the equator in this solution. The innermost shell is at  $r = 0.538$ , interior shell is at  $r = 1.221$ , and the outer shell at  $r = 1.538$ . The latitudinal circle where the tangent cylinder cuts the outer boundary is also shown. The solution is tilted forward  $15^\circ$ . Contours as in (a). (c) As (b) but for the azimuthal velocity  $u_\phi$ . In the outer part of the shell, eastward flow is dominant, in the inner region and at higher latitudes the flow is more westward. The azimuthal flow is also rather columnar. Black contours at  $u_\phi = 160$  and  $u_\phi = 480$ , white contour at  $u_\phi = -160$ . (d) The radial magnetic field  $B_r$ . Note the dipolar parity of the field which means  $B_r = 0$  on the equatorial plane. There is a substantial axisymmetric component, though the  $m = 7$  component is clearly visible near the interior shell. Black contours at  $B_r = 0.2$  and  $B_r = 0.6$ , white contours at  $B_r = -0.2$  and  $B_r = -0.6$ . (e) The azimuthal magnetic field  $B_\phi$ . This is almost entirely of one sign in the northern hemisphere (very small negative values do exist but at a value below the lowest contour level) and the opposite sign in the southern hemisphere. Note the 'invisible' azimuthal field is significantly stronger than the radial field at the surface. Black contours at  $B_\phi = 0.8$  and  $B_\phi = 2.4$ . (f) The meridional magnetic field  $B_\theta$ . This is not zero on the equatorial plane, but is surprisingly small there, except close to the inner core. Black contours at  $B_\theta = 0.3$  and  $B_\theta = 0.9$ , white contour at  $B_\theta = -0.3$ .

It proved to be quite difficult to find such solutions. The magnetic Reynolds number,  $Rm = U_0 d / \eta$ ,  $U_0$  being the root mean square velocity, must be quite large to give dynamo action, typically of order at least 100, and rapidly rotating convection typically has cha-

otic time-dependence at Rayleigh numbers not much above critical. The only possibility is therefore to have quite large magnetic Prandtl number, so that a large  $Rm$  can be achieved at moderate fluid Reynolds number  $Re = Rm / Pm$  and hence a Rayleigh

number not far above critical. Large  $Pm$  can however lead to computational difficulties, as small timesteps are necessary to resolve temporal variations of the flow field, while long integrations are necessary to ensure that the magnetic field has achieved its final state. The chosen benchmark is therefore necessarily a compromise, but because the steady drifting state has a well-defined and fairly large-scale structure, it can be computed without excessive computational resources.

In the actual rotating frame in which the computations are done, the solution is time-dependent. This means that the choice of timestep is important. Indeed, in compressible anelastic convection in spherical shells the drift speed is generally larger than in Boussinesq convection for reasons given in Jones et al. (2009) and Evonuk (2008), so accurate solutions typically require a somewhat smaller timestep than in the Boussinesq case.

With the parameters  $N_\rho = 3$ ,  $n = 2$ ,  $r_i/r_o = 0.35$ ,  $Pr = 1$ ,  $E = 0.002$  and stress-free boundaries, the first mode to become unstable has an azimuthal wavenumber  $m = 10$ , and occurs at  $Ra_{crit} = 61621.682$ . The corresponding frequency is  $\omega_m = 101.38\nu/d^2$  or  $\omega_m = 5069.0\eta/d^2$  on the magnetic diffusion timescale used here. In the nonlinear steady benchmark simulations, the  $m = 7$  mode was generally found. The onset for  $m = 7$  is at  $Ra = 65745.82$ ,  $\omega_m = 100.83\nu/d^2$ . The steady benchmark Rayleigh number at 80,000 is only about 1.3 times the critical Rayleigh number for the onset of convection. If the Rayleigh number is much greater than 1.3 times critical, the convection and the dynamo are unsteady.

A number of different initial conditions were tried which resulted in the  $m = 7$  steady drifting solution. Perhaps the simplest to implement are a zero initial velocity perturbation, a small random non-zero entropy perturbation, and a small random non-zero magnetic field perturbation. Provided the perturbations contain modes with all wavenumbers and no imposed symmetries, the exact nature of the perturbations seems not to be critical. An  $m = 7$  convection pattern emerged which leads to a dynamo which also has  $m = 7$  symmetry, that is only azimuthal modes which are integer multiples of 7 have non-zero amplitudes. All other modes decay away to zero. Although the solution has exact  $m = 7$  symmetry, this should not be imposed, as then the issue of whether the  $m = 7$  solution is stable to perturbations without this symmetry is not addressed. However, once the stability of the  $m = 7$  solution has been checked, imposing  $m = 7$  symmetry *a priori* will save computer time without affecting the accuracy of the results, when for example testing the effect of changing resolution or timestep.

The typical behaviour during the initial transient is that the convection settles to a mode which has  $m = 7$  dominant, but not with exact  $m = 7$  symmetry. Initially, the magnetic energy falls, but after about a quarter of a diffusion time (depending on the initial magnetic perturbation) an  $m = 7$  magnetic perturbation starts to grow exponentially. This  $m = 7$  perturbation takes some time to grow, the magnetic energy multiplying by a factor 10 in about 0.19 of the magnetic diffusion time, but eventually it affects the convection, and the nonlinear solution with exact  $m = 7$  symmetry emerges. We did not find any other dynamo solutions at these parameters other than the  $m = 7$  solution reported here. However, this is a complex nonlinear system, so we cannot be sure that other stable solutions do not exist.

All four codes tested found a steady solution with exact  $m = 7$  symmetry as shown in Fig. 2. The solution drifts with a uniform angular velocity, so all quantities have the form  $f(r, \theta, \phi - \omega t)$  with  $\omega = 2\pi/7\tau$  because of the sevenfold symmetry. In the coordinate frame the period is close to  $\tau = 1.467 \times 10^{-3}$  in the dimensionless units based on the magnetic diffusion time, corresponding to 2.412 days. The drift here is eastward while the Boussinesq dynamo benchmark (Christensen et al., 2001) drifts westward. The drift

speed of this anelastic compressible dynamo is significantly faster than the Boussinesq benchmark value. This pattern is rotating at 1/40.86 of the planetary rotation rate eastward. The Christensen benchmark rotated at 1/323 of the planetary rotation rate westward. For comparison, the linear theory gave  $\omega_m = 5069$  at the onset of convection in the dimensionless units when  $Ra = 61,622$  and  $m = 10$ . Because we write the wave form as  $\exp(im\phi - \omega_m t)$ ,  $\omega = \omega_m/10 = 506.9$ , slightly slower than our nonlinear drift frequency  $\omega = 611.9$ .

The form of the steady dynamo benchmark is shown in Fig. 2. Unlike the hydrodynamic benchmark, the  $m = 7$  convection pattern occurs over the whole equatorial plane, as shown in Fig. 2a. The density contrast is reduced to  $N_\rho = 3$  here compared to  $N_\rho = 5$  in the hydrodynamic case. Although the Ekman number is  $2 \times 10^{-3}$ , and so not very small compared with recently published Boussinesq dynamos (Kageyama et al., 2008; Sakuraba and Roberts, 2009; Jones, 2011) the convection is still columnar as can be seen in Fig. 2b and c. From Fig. 2c we see that the azimuthal flow is mainly eastward near the outer boundary and more westward in the interior. The radial component of magnetic field shows a dipolar symmetry (Fig. 2d). For the magnetic field, two equivalent solutions are possible that differ only in sign. The field may thus be dominantly outward in the northern and inward in the southern hemisphere (as shown in Fig. 2d), or the other way round. Which is found depends on the initial condition, but both of course have identical energies. There is a strong axisymmetric component to the magnetic field structure, particularly apparent near the poles in the radial component of the magnetic field (Fig. 2d) and everywhere in the azimuthal magnetic field (Fig. 2e). Note that the dipolar symmetry of the field means  $B_\phi$  is antisymmetric about the equator and hence exactly zero on the equatorial plane. The latitudinal component of the magnetic field (Fig. 2f) is symmetric about the equator and hence non-zero there. It is however surprisingly weak on the equatorial plane except very close to the inner boundary.

## 7. Unsteady dynamo benchmark

The hydrodynamic and steady dynamo benchmarks are quite close to critical, so the convective heat flux is less than the con-

**Table 5**  
Parameters for the unsteady dynamo benchmark.

<i>Dimensionless parameters</i>	
$E = 5 \times 10^{-5}$ , $N_\rho = 3$ , $\beta = 0.35$ , $Ra = 2.5 \times 10^7$ , $Pr = 2$ , $Pm = 2$ , $n = 2$	
<i>Defining physical input values</i>	
$r_o = 7 \times 10^9$ cm, $\Omega = 1.76 \times 10^{-4}$ s $^{-1}$ , $M = 1.9 \times 10^{30}$ g, $\rho_i = 1.1$ g cm $^{-3}$ , $\mathcal{R} = 3.503 \times 10^7$ erg g $^{-1}$ K $^{-1}$ , $G = 6.67 \times 10^{-8}$ g $^{-1}$ cm $^3$ s $^{-2}$	
<i>Polytropic constants</i>	
$\zeta_0 = 0.525580$ , $\zeta_i = 2.355486$ , $c_0 = -0.459754$ , $c_1 = 1.515898$ , $V = 14.598801$	
<i>Derived physical input values</i>	
$r_i = 2.45 \times 10^9$ cm, $d = 4.55 \times 10^9$ cm, $\nu = 1.82182 \times 10^{11}$ cm $^2$ s $^{-1}$ , $\kappa = 9.1091 \times 10^{10}$ cm $^2$ s $^{-1}$ , $\eta = 9.1091 \times 10^{10}$ cm $^2$ s $^{-1}$	
<i>Derived thermodynamic quantities in the model</i>	
$\rho_c = 0.198258$ g cm $^{-3}$ , $\rho_o = 0.0547658$ g cm $^{-3}$ , $T_i = 411,829$ K, $T_c = 174,838$ K, $T_o = 91891.5$ K, $p_i = 1.586901 \times 10^{13}$ dyne cm $^{-2}$ , $p_c = 1.214251 \times 10^{12}$ dyne cm $^{-2}$ , $p_o = 1.762888 \times 10^{11}$ dyne cm $^{-2}$ , $\Delta S = 7.56121 \times 10^4$ erg g $^{-1}$ K $^{-1}$ , $c_p = 1.0509 \times 10^8$ erg g $^{-1}$ K $^{-1}$ , $\Delta S/c_p = 0.0007195$	
Basic state luminosity = $1.2031317 \times 10^{31}$ erg s $^{-1}$	
<i>Dimensionless units</i>	
Velocity 20.02 cm s $^{-1}$ ; time 2.272727 $\times 10^8$ s; distance $4.55 \times 10^9$ cm; energy $7.485038 \times 10^{30}$ erg; Energy density $79.462060$ erg cm $^{-3}$ ; luminosity $1.086292 \times 10^{30}$ erg s $^{-1}$ ; magnetic field 6319.967 G	

**Table 6**  
Results from the unsteady dynamo benchmark. Time-averaged values are shown, with the corresponding standard deviation in square brackets, expressed as a percentage of the average value.

Code	Leeds	Glatzmaier	ASH	MAGIC
M.E. (erg)	$1.81 \times 10^{36}$ [12%]	$1.80 \times 10^{36}$ [10%]	$1.77 \times 10^{36}$ [13%]	$1.84 \times 10^{36}$ [11%]
M.E. dimensionless	$2.42 \times 10^5$ [12%]	$2.40 \times 10^5$ [10%]	$2.37 \times 10^5$ [13%]	$2.46 \times 10^5$ [11%]
K.E. (erg)	$1.74 \times 10^{36}$ [13%]	$1.75 \times 10^{36}$ [12%]	$1.72 \times 10^{36}$ [12%]	$1.74 \times 10^{36}$ [12%]
K.E. dimensionless	$2.32 \times 10^5$ [13%]	$2.34 \times 10^5$ [12%]	$2.29 \times 10^5$ [12%]	$2.32 \times 10^5$ [12%]
Zonal M.E. (erg)	$7.07 \times 10^{34}$ [40%]	$7.07 \times 10^{34}$ [38%]	$7.12 \times 10^{34}$ [34%]	$7.10 \times 10^{34}$ [41%]
Zonal M.E. dimensionless	$9.45 \times 10^3$ [40%]	$9.45 \times 10^3$ [38%]	$9.51 \times 10^3$ [34%]	$9.49 \times 10^3$ [41%]
Meridional M.E. (erg)	$1.59 \times 10^{35}$ [43%]	$1.66 \times 10^{35}$ [33%]	$1.53 \times 10^{35}$ [38%]	$1.67 \times 10^{35}$ [44%]
Meridional M.E. dimensionless	$2.13 \times 10^4$ [43%]	$2.22 \times 10^4$ [33%]	$2.04 \times 10^4$ [38%]	$2.23 \times 10^4$ [44%]
Zonal K.E. (erg)	$1.02 \times 10^{35}$ [37%]	$1.00 \times 10^{35}$ [43%]	$1.02 \times 10^{35}$ [55%]	$1.02 \times 10^{35}$ [38%]
Zonal K.E. dimensionless	$1.36 \times 10^4$ [37%]	$1.34 \times 10^4$ [43%]	$1.36 \times 10^4$ [55%]	$1.36 \times 10^4$ [38%]
Meridional K.E. (erg)	$7.84 \times 10^{32}$ [31%]	$8.36 \times 10^{32}$ [30%]	$8.90 \times 10^{32}$ [29%]	$8.28 \times 10^{32}$ [32%]
Meridional K.E. dimensionless	105 [31%]	112 [30%]	119 [29%]	111 [32%]
Luminosity (erg s <sup>-1</sup> )	$4.62 \times 10^{31}$	$4.67 \times 10^{31}$	$4.65 \times 10^{31}$	$4.64 \times 10^{31}$
Luminosity dimensionless	42.5	43.0	42.8	42.7
Standard deviation (bottom)	11%	11%	9%	11%
Standard deviation (top)	4%	4%	3%	5%
Resolution	$96 \times 288 \times 576$	$129 \times 256 \times 512$	$129 \times 256 \times 512$	$121 \times 256 \times 512$
Timestep (s)	681	100	100	113.64
Timestep dimensionless	$3 \times 10^{-6}$	$4.4 \times 10^{-7}$	$4.4 \times 10^{-7}$	$5 \times 10^{-7}$
Run length (days)	3950	1022	2014	3644
Run length dimensionless	1.5	0.39	0.77	1.35

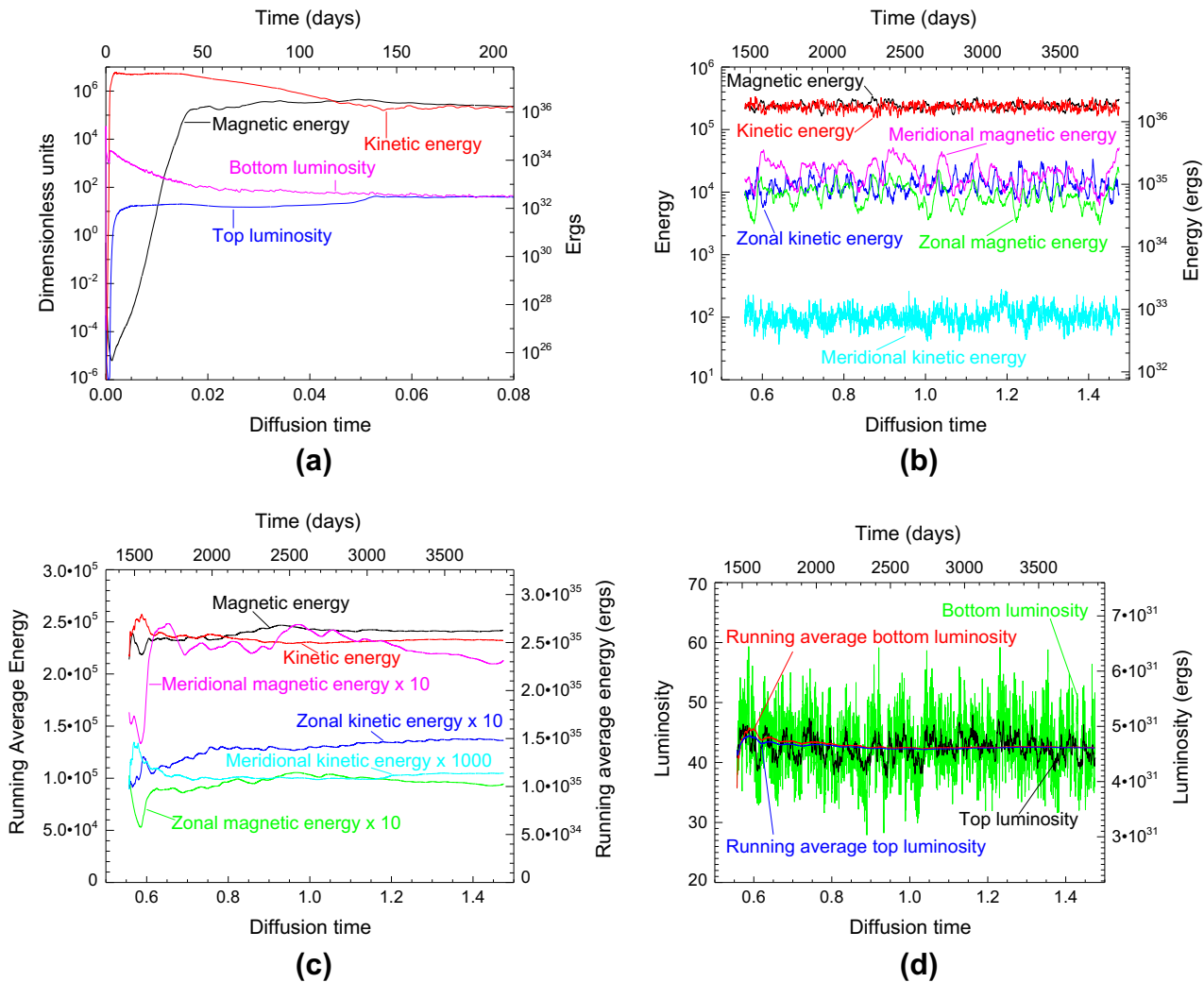


**Fig. 3.** Energies and luminosities of the unsteady benchmark. (a) The magnetic and kinetic energies and the top and bottom luminosities during the initial transient. (b) The magnetic and kinetic energies for one diffusion time after saturation. Also shown are the azimuthally averaged zonal magnetic and kinetic energies and meridional magnetic and kinetic energies. (c) The running average of those energies. (d) The top and bottom luminosities and their running averages.

ducted heat flux, Nusselt numbers being 1.062 and 1.039 respectively. To test the codes at higher critical  $Ra$ , in a situation where the convective heat flux is significantly larger than the conducted flux, we examined an unsteady dynamo benchmark with parameters given in Table 5. The price paid for increasing  $Ra$  to well above critical is that the solutions become unsteady, indeed mildly turbu-

lent, so that only averaged values of kinetic and magnetic energy, and luminosity, can be found. Because it is only practical to integrate at higher Rayleigh numbers for at most a few diffusion times, computed averages will not have completely settled by the end of the run, so we cannot expect the same accuracy levels as are possible for the benchmarks which are steady in a drifting frame.

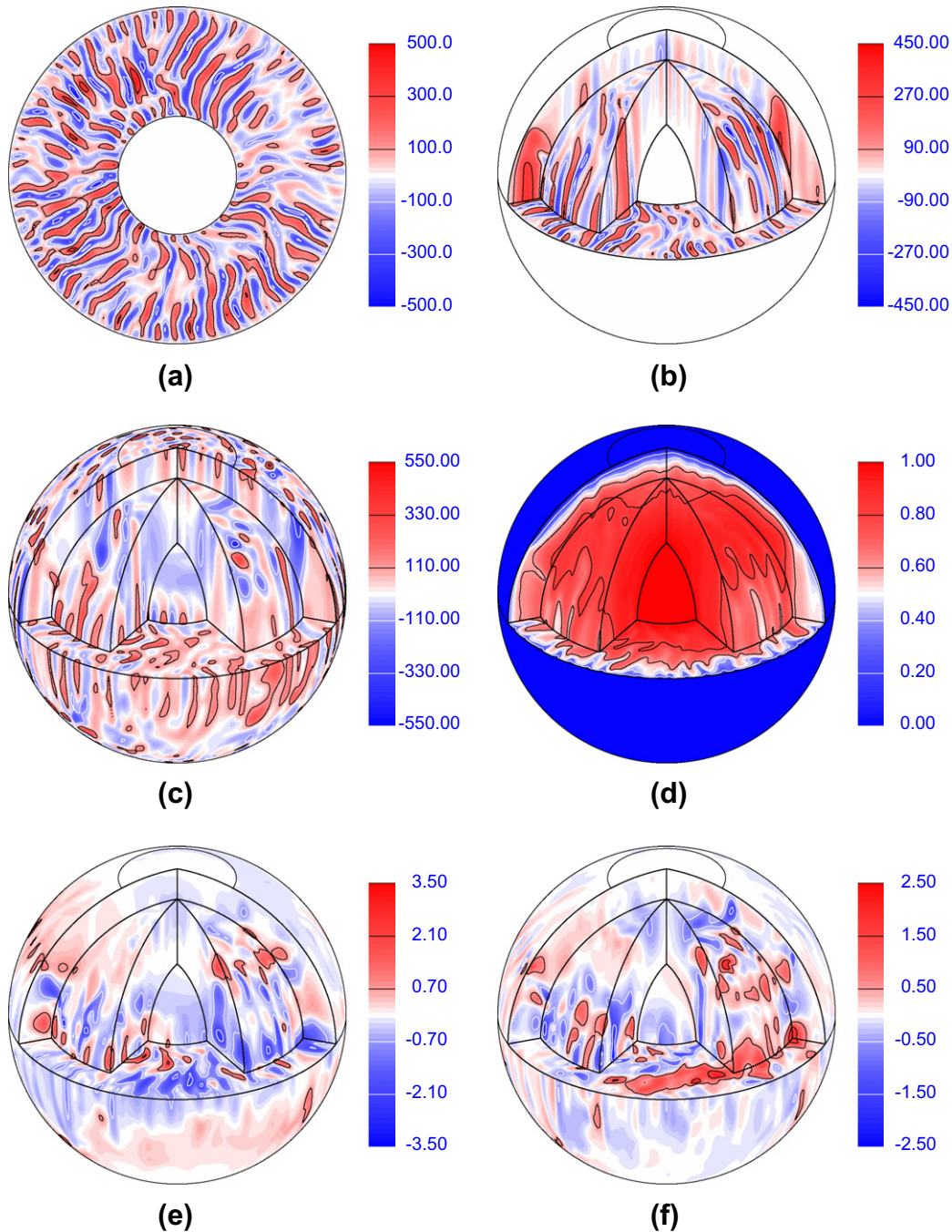


**Fig. 4.** Unsteady dynamo benchmark snapshots. Dimensionless units throughout. (a) Radial velocity in the equatorial plane. The low Ekman number leads to thin velocity structures. Black contours at  $u_r = 100$  and  $u_r = 300$ , white contours at  $u_r = -100$  and  $u_r = -300$ . (b) Cut-away plot of the radial velocity. Despite the chaotic nature of the flow in the equatorial plane, the flow is still columnar. There is some convection inside the tangent cylinder, but it is weak. The innermost shell is at  $r = 0.538$ , interior shell is at  $r = 1.221$ , and the outer shell at  $r = 1.538$ . The solution is tilted forward  $30^\circ$ . Contours as in (a). (c) As (b) but for the azimuthal velocity  $u_\phi$ . Near the equatorial plane the eastward flow is dominant, but near the tangent cylinder westward flow occurs. The azimuthal flow is also rather columnar. Black contours at  $u_\phi = 110$  and  $u_\phi = 330$ , white contours at  $u_\phi = -110$  and  $u_\phi = -330$ . (d) The entropy. The convection has created a thermal boundary layer near the outer boundary, across which the entropy drops rapidly. White contours at  $S = 0.2, 0.4$ , black contours at  $S = 0.6, 0.8$ . (e) The radial magnetic field  $B_r$ . This is rather irregular and there is no clear dipole (or quadrupole) parity. There are a few large scale patches of field, but they do not persist in time. Black contours at  $B_r = 0.7$  and  $B_r = 2.1$ , white contours at  $B_r = -0.7$  and  $B_r = -2.1$ . (f) The azimuthal magnetic  $B_\phi$ . Like the radial field this has no persistent large scale structure. Unlike the steady benchmark dynamo, the azimuthal field is not stronger than the radial field. Black contours at  $B_\phi = 0.5$  and  $B_\phi = 1.5$ , white contours at  $B_\phi = -0.5$  and  $B_\phi = -1.5$ .

The procedure adopted for the time average and standard deviations listed in Table 6 was to start from a small thermal and magnetic perturbation, until the large initial transients disappear (see Fig. 3a). Then the solution was integrated for a further settling time, typically about half a magnetic diffusion time, and then the averaging process was started, over the data shown in Fig. 3b (energies) and 3d (luminosities). As can be seen from these figures, the energies continually fluctuate randomly with an amplitude of about 10%, so to give some indication of whether the average values are settling we plot the running averages in Fig. 3c. The running average kinetic energy is defined as

$$AKE(t) = \frac{1}{t - t_0} \int_{t_0}^t \int_V \frac{1}{2} \rho \mathbf{u}^2 r^2 \sin \theta dr d\theta d\phi dt \quad (37)$$

where  $t_0$  is the point at which the averaging starts, which for Fig. 3 was  $t_0 = 0.557$  in units of the magnetic diffusion time. Running averages for other quantities are defined similarly. It appears as though the magnetic and kinetic energies do settle to well-defined values, but it would require a very long (and expensive) time-integration to get these values to significantly better than 1% accuracy. Similarly, the running average of the luminosity emerging from the top boundary should approach the luminosity flowing into the bottom boundary, as there are no internal heat sources. We see in Fig. 3d that this does happen, but that it takes a long time for equality to establish.

The onset of convection for the unsteady benchmark parameter values occurs with an  $m = 43$  mode at  $Ra = 9.33002 \times 10^6$ , with  $\omega_m = 590.12\nu/d^2$ , which corresponds to  $\omega_m = 1180.24$  in our dimensionless units. The unsteady benchmark Rayleigh number is therefore 2.68 times the critical value for the onset of convection.

In Table 6 we give the results for the averages found by the various groups for this unsteady benchmark, giving as before both dimensional and dimensionless values to facilitate comparison between codes. We also give the standard deviation of the energy of the run, defined as

$$\sigma = \left( \frac{1}{t_f - t_0} \int_{t_0}^{t_f} (E - \bar{E})^2 dt \right)^{1/2}, \quad (38)$$

where  $\bar{E}$  is the average energy over the whole run between  $t_0$  and  $t_f$ . Note that  $t_0$  should be chosen large enough for the effects of initial transients to be removed. It is even harder to establish precise values for the standard deviations than for the average energies themselves, so these standard deviations are only included to give some estimate of the amount of fluctuation to be expected.

The form of the solution for the unsteady dynamo benchmark can be seen in the snapshots shown in Fig. 4. Unlike the solutions shown in Figs. 1 and 2, the flow and field patterns vary considerably with time, so these are only typical of the behaviour; researchers should not be unduly concerned if their equivalent plots differ somewhat from these. The low value of  $E = 5 \times 10^{-5}$  leads to thin convection columns, visible in the radial velocity Fig. 4a and b. Convection occurs both inside and outside the tangent cylinder, but at these parameters it is weaker inside the tangent cylinder. There is significant differential rotation, strongly eastward in the equatorial plane, westward at higher latitudes. In Fig. 4d we see that the entropy has been affected by the convection, as expected with larger Nusselt numbers; the average Nusselt number for the unsteady dynamo benchmark is around 3.9. The entropy is still fairly close to the inner boundary value except near the outer boundary. The magnetic field shows no persistent large scale structure, unlike the steady dynamo benchmark. Patches of large scale field, both radial and azimuthal, can be seen in Fig. 4e and f, but they come and go in different locations as time increases. Despite this, the overall magnetic energy reaches a fairly well-defined average value (Fig. 3c) and even the

azimuthally averaged zonal and meridional fields approach well-defined limiting values.

## 8. Discussion and conclusions

Once the benchmark cases were formulated, a number of difficulties were experienced before the agreement found in Tables 2, 4 and 6 was obtained. The main issue concerned angular momentum conservation, which is a problem specific to the choice of stress-free boundaries. If we take the vector product of Eq. (2) with  $\mathbf{r}$  and integrate over the whole shell volume, we find that all three components of the total angular momentum are conserved, see Appendix A where formulae for the components of the angular momentum and the magnetic torques are given. The truncation errors in space and time associated with the numerical methods mean that at each timestep there is a small change in the angular momentum. Since the numerical schemes we used are well resolved both spatially and temporally, this error is small for each timestep, but the cumulative effect when integrating over very large numbers of steps can be non-negligible. Since the dynamo equations have to be integrated over many turnover times before they settle, this is a very real hazard. We found that when no special measures were employed to ensure accurate angular momentum conservation were in place, small growth of the angular momentum could lead to significant errors developing in the energy. It is particularly important to ensure that the equatorial  $x$  and  $y$  components of angular momentum remain zero, not just the axial  $z$  component, as these equatorial components correspond to a rotation which advects polar fluid (where the magnetic field may be coherent and strong) to the equator and thus can lead to a large (erroneous) growth of magnetic field as it gets stretched out by equatorial differential rotation.

Once the problem has been identified, the solution is quite straightforward. Either one stress-free boundary condition can be replaced by the global condition that angular momentum is exactly conserved at each timestep, or the angular momentum can be computed explicitly at each timestep and an appropriate solid body rotation added to remove any angular momentum change. In spectral codes, both of these conditions are easy to implement, because the angular momentum only affects a few spherical harmonics (see Appendix A). Although this problem surfaced in the context of anelastic convection, the Boussinesq case with stress-free boundaries will give rise to similar problems. Normally, no-slip conditions have been used in Boussinesq simulations (as in the 2001 benchmark) motivated by convection in liquid metal cores, where there is a solid core-mantle boundary.

The issue of angular momentum conservation, and the serious errors that can arise over long integration times when stress-free boundaries are used, is an important lesson from these studies. In practice, there is always a compromise between keeping the timestep small to obtain reasonable accuracy but not so small that long overall integration times become impossibly expensive. It is therefore not usually practical to keep the timestep small enough to conserve angular momentum with the required degree of accuracy, so additional measures have to be taken to ensure accurate conservation of all three components of the angular momentum vector.

Researchers whose experience is with Boussinesq codes may also be surprised at the magnitude of the truncation errors incurred by having too large a timestep. With Boussinesq codes, provided the timestep is small enough to ensure numerical stability, truncation errors are usually sufficiently small that even a first order integration scheme gives sufficient accuracy. The faster wave

propagation in compressible rotating convection means that reducing the timestep until stability is found is not necessarily sufficient, particularly if accurate agreement with the benchmark is desired. A timestep significantly below the stability limit may be needed. We have not performed a systematic analysis on this point, but we did find that runs with the timestep controlled only by stability considerations were significantly less accurate than those reported in the tables given here. The Leeds and Glatzmaier codes were stable with timesteps at least three times larger than those quoted in Table 4, and though the results at the larger timesteps only differed by less than 1%, this was significantly greater than the final accuracy achieved.

The overall level of agreement between the codes is very satisfactory, giving considerable confidence that these benchmark solutions are a reliable test for newly developed codes. Of course, it should be borne in mind that the benchmark solutions are low Rayleigh number, moderately small Ekman number solutions, with  $N_\rho$  not too large. Consequently, even our unsteady case is not turbulent enough, or rotationally dominant enough, to maintain a banded pattern of alternating east–west directed zonal jets as seen on the surface of Jupiter and Saturn. However, banded patterns do emerge at much higher  $Ra$  and smaller  $E$ , see e.g. Jones and Kuzanyan (2009). We spent a considerable amount of time looking for benchmark cases that require only modest computer resources. More extreme values of any of these parameters would reduce the accuracy of the solutions. Also, a benchmark at more extreme values could only be statistical in nature, and would certainly require far larger computing resources than are needed for the benchmarks presented here.

## Acknowledgments

We are grateful to the Kavli Institute of Theoretical Physics, University of California at Santa Barbara, for funding the programme on *Dynamo theory: Magnetic field generation in experiments, planets, stars, disks and galaxies* in 2008 at which the anelastic benchmark proposal was formulated.

Use was made of the following computational facilities during this work: the University of Leeds High Performance Computing Cluster; the University of St. Andrews computer cluster funded by the UK Research Council, STFC; the GWDG computer facility in Germany; the French GENCI supercomputing centre; the University of California Shared Research Computing Service; the NSF PACI support at the Teragrid sites of NICS, TACC, and NCSA; the NASA Ames Research Center.

P.B. was grateful for support from STFC, Grant No. PP/E001092/1. T.G. was supported by the Special Priority Program 1488 (PlanetMag) of the German Science Foundation. G.A.G. was supported by NASA Grants NNX09AD89G and NNX11AB46G, M.S.M. by NASA Grants NNX09AK14I-SHP and NNX08AI57G-HTP, and A.S.B. by ERC-Stg Grant 207430 STARS2, and by the CNRS/INSU Programmes Nationaux Soleil-Terre and Physique Stellaire.

## Appendix A

Angular momentum is most easily treated in a non-rotating frame, in which the velocity  $\tilde{\mathbf{u}}$  is

$$\tilde{\mathbf{u}} = \mathbf{u} + \boldsymbol{\Omega} \times \mathbf{r}. \quad (\text{A1})$$

Since the solid body rotation term  $\boldsymbol{\Omega} \times \mathbf{r}$  has no stress at the boundaries,  $\tilde{\mathbf{u}}$  satisfies the stress-free boundary conditions and Eq. (2) without the Coriolis term. The centrifugal acceleration term is neglected in (2) in comparison with gravity, as usual in spherical convection studies.

Taking the vector product of  $\mathbf{r}$  with the equation of motion and integrating over the whole shell volume gives

$$\begin{aligned} & \int \mathbf{r} \times \bar{\rho} \frac{\partial \tilde{\mathbf{u}}}{\partial t} dv + \int \mathbf{r} \times \bar{\rho} (\tilde{\mathbf{u}} \cdot \nabla) \tilde{\mathbf{u}} dv \\ &= - \int \mathbf{r} \times \nabla p' dv + \int \mathbf{r} \times (\mathbf{j} \times \mathbf{B}) dv + \int \mathbf{r} \times \bar{\rho} \mathbf{F}_v dv. \end{aligned} \quad (\text{A2})$$

The angular momentum is then

$$\int \mathbf{r} \times \bar{\rho} \tilde{\mathbf{u}} dv = \mathbf{L}_0 + \mathbf{L}' \quad (\text{A3})$$

where

$$\mathbf{L}_0 = \frac{8\pi\hat{\mathbf{z}}}{3} \int_{r_i}^{r_o} \Omega \bar{\rho} r^4 dr, \quad (\text{A4})$$

is the fixed contribution from the basic state and

$$\begin{aligned} L'_x &= \int -\bar{\rho} (r \sin \phi u_\theta + r \cos \theta \cos \phi u_\phi) dv, \\ L'_y &= \int \bar{\rho} (r \cos \phi u_\theta - r \cos \theta \sin \phi u_\phi) dv, \end{aligned} \quad (\text{A5, A6})$$

$$L'_z = \int \bar{\rho} r \sin \theta u_\phi dv, \quad (\text{A7})$$

are the three Cartesian components of the angular momentum due to the convection. With stress-free and magnetically insulating boundaries all these contributions to the total angular momentum must remain fixed, as we show below. Within the framework of the anelastic approximation, the fluctuation of  $\mathbf{L}_0$  due to the density perturbation  $\rho'$  is small compared to the magnitude of  $\mathbf{L}'$ . If the velocity is expanded in toroidal and poloidal components, as is usual in the spectral approaches,

$$\mathbf{u} = \frac{1}{\bar{\rho}} \nabla \times \nabla \times \mathbf{r} P \bar{\rho} + \frac{1}{\bar{\rho}} \nabla \times \mathbf{r} T \bar{\rho}, \quad (\text{A8})$$

then the poloidal part gives zero contribution to the angular momentum. To see this, we note that we can express the integrand as a divergence since using suffix notation

$$\begin{aligned} \mathbf{r} \times \nabla \times \nabla \times \mathbf{r} P \bar{\rho} &= \epsilon_{ijk} r_j \left( \frac{\partial (r_m \bar{\rho} P)}{\partial x_k \partial x_m} - \frac{\partial (r_k \bar{\rho} P)}{\partial x_m \partial x_m} \right) \\ &= \frac{\partial}{\partial x_m} \left( \epsilon_{ijk} r_j \left[ \frac{\partial (r_m P \bar{\rho})}{\partial x_k} - \frac{\partial (r_k P \bar{\rho})}{\partial x_m} \right] + 2 \epsilon_{imk} r_k P \bar{\rho} \right). \end{aligned} \quad (\text{A9})$$

The angular momentum volume integral can then be written as the difference of surface integrals,

$$\begin{aligned} & \int_{S_{out}} \epsilon_{ijk} r_j \left( \frac{\partial (r_m P \bar{\rho})}{\partial x_k} - \frac{\partial (r_k P \bar{\rho})}{\partial x_m} \right) \hat{r}_m dS \\ & - \int_{S_{in}} \epsilon_{ijk} r_j \left( \frac{\partial (r_m P \bar{\rho})}{\partial x_k} - \frac{\partial (r_k P \bar{\rho})}{\partial x_m} \right) \hat{r}_m dS, \end{aligned} \quad (\text{A10})$$

$\hat{\mathbf{r}}$  being the unit vector in the radial direction. The last term in (A9) gives zero contribution because of the antisymmetry of  $\epsilon_{ijk}$ . These surface integrals both vanish, because  $u_r = 0$  on the boundaries implies that  $P = 0$ , and hence  $\mathbf{r} \times \nabla P = 0$  on the boundaries. The toroidal part of the velocity gives non-zero angular momentum, but if  $T$  is expanded in spherical harmonics with complex coefficients,

$$T = \sum_{l=1}^{\infty} \sum_{m=-l}^{m=l} T_{lm}(r) P_l^{|m|}(\cos \theta) e^{im\phi} \quad (\text{A11})$$

with  $T_{l,-m} = T_{l,m}^*$ , \* denoting complex conjugate, then only the  $T_{10}$  and  $T_{11}$  coefficients appear in the expressions for  $\mathbf{L}'$ , and the components are

$$\begin{aligned}
L'_x &= \frac{16\pi}{3} \int_{r_i}^{r_o} \operatorname{Re}\{T_{11}(r)\} \bar{\rho} r^3 dr, \\
L'_y &= -\frac{16\pi}{3} \int_{r_i}^{r_o} \operatorname{Im}\{T_{11}(r)\} \bar{\rho} r^3 dr, \\
L'_z &= \frac{8\pi}{3} \int_{r_i}^{r_o} T_{10}(r) \bar{\rho} r^3 dr,
\end{aligned} \tag{A12, A13, A14}$$

where  $\operatorname{Re}\{\}$  denotes the real part and  $\operatorname{Im}\{\}$  denotes the imaginary part,  $T_{10}(r)$  being purely real. This makes it particularly convenient to evaluate the angular momentum with spectral codes.

The vanishing of the viscous force term in (A2) is an immediate consequence of it being the divergence of the viscous stress-tensor, and the relevant components of the stress tensor vanish on the spherical boundaries because of the stress-free conditions there. Similarly, the vanishing of the pressure gradient torque is a simple consequence of writing this term as a divergence and applying  $u_r = 0$  on the boundaries. The vanishing of the Reynolds stress term is a consequence of (4), since then

$$\begin{aligned}
\int \bar{\rho} \epsilon_{ijk} r_j \tilde{u}_m \frac{\partial}{\partial x_m} \tilde{u}_k dv &= \int \frac{\partial}{\partial x_m} (\epsilon_{ijk} \bar{\rho} r_j \tilde{u}_k \tilde{u}_m) - \epsilon_{ijk} \bar{\rho} \tilde{u}_j \tilde{u}_k dv \\
&= \int_S \epsilon_{ijk} \bar{\rho} r_j \tilde{u}_k \tilde{u}_m \hat{r}_m dS,
\end{aligned} \tag{A15}$$

and the inner and outer surface integrals are zero because  $\tilde{\mathbf{u}} \cdot \hat{\mathbf{r}} = 0$  on the boundaries.

The vanishing of the Lorentz term is more involved than one might expect, see Rochester (1962). The Lorentz torque can be expressed as a divergence involving the Maxwell stresses,

$$\Gamma = \int \mathbf{r} \times (\mathbf{j} \times \mathbf{B}) dv = \int \frac{\partial}{\partial x_m} \left( \epsilon_{ijk} r_j (B_k B_m - \frac{1}{2} \delta_{km} \mathbf{B}^2) \right) dv. \tag{A16}$$

The magnetic torque can then be written as surface integrals (Rochester, 1962)

$$\begin{aligned}
\Gamma_x &= \int_{S_{out}} -(r \sin \phi B_r B_\theta + r \cos \theta \cos \phi B_r B_\phi) dS \\
&\quad + \int_{S_{in}} (r \sin \phi B_r B_\theta + r \cos \theta \cos \phi B_r B_\phi) dS,
\end{aligned} \tag{A17}$$

$$\begin{aligned}
\Gamma_y &= \int_{S_{out}} (r \cos \phi B_r B_\theta - r \cos \theta \sin \phi B_r B_\phi) dS \\
&\quad - \int_{S_{in}} (r \cos \phi B_r B_\theta - r \cos \theta \sin \phi B_r B_\phi) dS,
\end{aligned} \tag{A18}$$

$$\Gamma_z = \int_{S_{out}} r \sin \theta B_r B_\phi dS - \int_{S_{in}} r \sin \theta B_r B_\phi dS, \tag{A19}$$

the surface integrals being the difference of the outer sphere and inner sphere contributions. With perfectly conducting boundaries,  $B_r = 0$  and the vanishing of all three components is evident. With insulating boundaries it is not quite so simple. Expressing the magnetic field in toroidal and poloidal scalars,

$$\mathbf{B} = \nabla \times \nabla \times \mathbf{rP} + \nabla \times \mathbf{rT}, \tag{A20}$$

the insulating conditions imply that  $T = 0$  on both boundaries and  $(\partial_r - l/r)P = 0$  on  $r = r_i$  and  $(\partial_r + (l+1)/r)P = 0$  on  $r = r_o$ , where  $l$  refers to the components of  $P$  with spherical harmonic degree  $l$ . On inserting these into (A17)–(A19) it is clear that the toroidal part gives zero contribution, since  $T$  and hence its horizontal derivatives are zero on the boundaries. The poloidal expansion can be written

$$P = \sum_{l=1}^{\infty} \sum_{m=-l}^{m=l} \mathcal{P}_{lm}(r) P_l^{lm}(\cos \theta) e^{im\phi}. \tag{A21}$$

The expression for  $\Gamma_z$  from the outer surface is then

$$\begin{aligned}
\Gamma_z^{out} &= \int_{S_{out}} \sum_{l=1}^{\infty} \sum_{m=-l}^{m=l} l(l+1) P_l^{lm}(\cos \theta) \mathcal{P}_{lm} e^{im\phi} \sum_{l'=1}^{\infty} \\
&\quad \times \sum_{m'=-l'}^{m'=l'} P_{l'}^{m'l}(\cos \theta) \frac{im'}{r} \frac{\partial}{\partial r} (r \mathcal{P}_{l'm'}) e^{im'\phi} dS.
\end{aligned} \tag{A22}$$

The orthogonality of the spherical harmonics implies that only contributions with  $l = l'$  and  $m = -m'$  are non-zero, and  $m = 0$  gives nothing. Using the boundary condition on the outer surface, the contribution to  $\Gamma_z$  there is

$$\int_{S_{out}} \sum_{l=1}^{\infty} \sum_{m=1}^l l(l+1) [P_l^{lm}(\cos \theta)]^2 \mathcal{P}_{lm} \mathcal{P}_{lm}^* \left( \frac{iml}{r} - \frac{iml}{r} \right) dS = 0. \tag{A23}$$

since the contributions from  $m$  and  $-m$  in the sum cancel out. A similar argument holds on the inner surface. To establish the  $x$  and  $y$  components of the Lorentz torque vanish, we note that the Lorentz force, unlike rotational forces, has no preferred direction. We can therefore simply make the transformation  $x' = y$ ,  $y' = z$  and  $z' = x$ , with corresponding spherical polar coordinates  $r'$ ,  $\theta'$  and  $\phi'$ . Then  $\Gamma_x$  takes exactly the same form in the primed coordinates as  $\Gamma_z$  does in the original coordinates. We then expand  $\mathbf{B}$  in poloidal and toroidal scalars in the primed coordinates, and expand  $\mathcal{P}'$  in spherical harmonics based on the primed coordinate system. Since the boundary conditions only involve  $r$  and  $r$ -derivatives, these are unchanged in the new primed system, and so  $\Gamma_x = \Gamma'_x = 0$  by the same argument, and a similar argument shows  $\Gamma_y = 0$ .

## References

- Braginsky, S.I., Roberts, P.H., 1995. Equations governing convection in Earth's core and the geodynamo. *Geophys. Astrophys. Fluid Dynam.* 79, 1–97.
- Brun, A.S., Miesch, M.S., Toomre, J., 2004. Global-scale turbulent convection and magnetic dynamo action in the solar envelope. *Astrophys. J.* 614, 1073–1098.
- Chandrasekhar, S., 1961. *Hydrodynamic and Hydromagnetic Stability*. Clarendon Press, Oxford.
- Christensen, U.R. et al., 2001. A numerical dynamo benchmark. *Phys. Earth Planet. Inter.* 128, 25–34.
- Clune, T.C., Elliot, J.R., Miesch, M., Toomre, J., Glatzmaier, G.A., 1999. Computational aspects of a code to study rotating turbulent convection in spherical shells. *Parallel Comput.* 25, 361–380.
- Evonuk, M., 2008. The role of density stratification in generating zonal flow structures in a rotating fluid. *Astrophys. J.* 673, 1154–1159.
- Gilman, P.A., Glatzmaier, G.A., 1981. Compressible convection in a rotating spherical shell. I – Anelastic equations. *Astrophys. J. Suppl. Ser.* 45, 335–349.
- Glatzmaier, G.A., 1984. Numerical simulations of stellar convective dynamos. I. The model and method. *J. Comput. Phys.* 55, 461–484.
- Glatzmaier, G.A., 1985. Numerical simulations of stellar convective dynamos. II – Field propagation in the convection zone. *Astrophys. J.* 291, 300–307.
- Glatzmaier, G.A., Gilman, P.A., 1981. Compressible convection in a rotating spherical shell. IV – Effects of viscosity, conductivity, boundary conditions, and zone depth. *Astrophys. J. Suppl. Ser.* 47, 103–115.
- Gough, D.O., 1969. The anelastic approximation for thermal convection. *J. Atmos. Sci.* 26, 448–456.
- Iskakov, A., Dormy, E., 2005. On magnetic boundary conditions for non-spectral dynamo simulations. *Geophys. Astrophys. Fluid Dynam.* 99, 481–492.
- Jones, C.A., 2011. Planetary magnetic fields and fluid dynamos. *Ann. Rev. Fluid Mech.* 43, 583–614.
- Jones, C.A., Kuzanyan, K.M., 2009. Compressible convection in the deep atmospheres of giant planets. *Icarus* 204, 227–238.
- Jones, C.A., Kuzanyan, K.M., Mitchell, R.H., 2009. Linear theory of compressible convection in rapidly rotating spherical shells, using the anelastic approximation. *J. Fluid Mech.* 634, 291–319.
- Kageyama, A., Miyagoshi, T., Sato, T., 2008. Formation of current coils in geodynamo simulations. *Nature* 454, 1106–1109.
- Kaspi, Y., Flierl, G.R., Showman, A.P., 2009. The deep wind structure of the giant planets: Results from an anelastic general circulation model. *Icarus* 202, 525–542.
- Landau, L.D., Lifshitz, E.M., 1959. *Fluid Mechanics*, Pergamon Press.
- Lantz, S.R., 1992. *Dynamical Behavior of Magnetic Fields in a Stratified, Convecting Fluid Layer*. Ph.D. Thesis, Cornell University.
- Lantz, S.R., Fan, Y., 1999. Anelastic magnetohydrodynamic equations for modeling solar and stellar convection zones. *Astrophys. J. Suppl. Ser.* 121, 247–264.
- Miesch, M.S., 2005. Large-scale dynamics of the convection zone and tachocline. *Living Rev. Solar Phys.* 2, 1. <<http://www.livingreviews.org/lrsp-2005-1>> (cited on 8th August 2011).

- Miesch, M.S., Elliott, J.R., Toomre, J., Clune, T.C., Glatzmaier, G.A., Gilman, P.A., 2000. Three-dimensional spherical simulations of solar convection: Differential rotation and pattern evolution achieved with laminar and turbulent states. *Astrophys. J.* 532, 593–615.
- Ogura, Y., Phillips, N.A., 1962. Scale analysis of deep and shallow convection in the atmosphere. *J. Atmos. Sci.* 19, 173–179.
- Roberts, P.H., 2007. Theory of the geodynamo. In: Olson, P. (Ed.), *Treatise of Geophysics*, Schubert, G. (series Ed.), vol. 8. Elsevier.
- Rochester, M.G., 1962. Geomagnetic core–mantle coupling. *J. Geophys. Res.* 67, 4833–4836.
- Sakuraba, A., Roberts, P.H., 2009. Generation of a strong magnetic field using uniform heat flux at the surface of the core. *Nat. Geosci.* 2, 802–805.